Bachelor's project

NTNU
Norwegian University of Science and Technology
Faculty of Engineering
Department of Mechanical and Industrial Engineering

Kristoffer Finnson
Fredrik Nes Fredheim
Andreas Inderberg

Simulation of Shock and Vibration Forces for Space-based Components

Bachelor's project in Mechanical Engineering
Supervisor: Cecilia Haskins
Co-supervisor: Evelyn Honoré-Livermore

May 2021

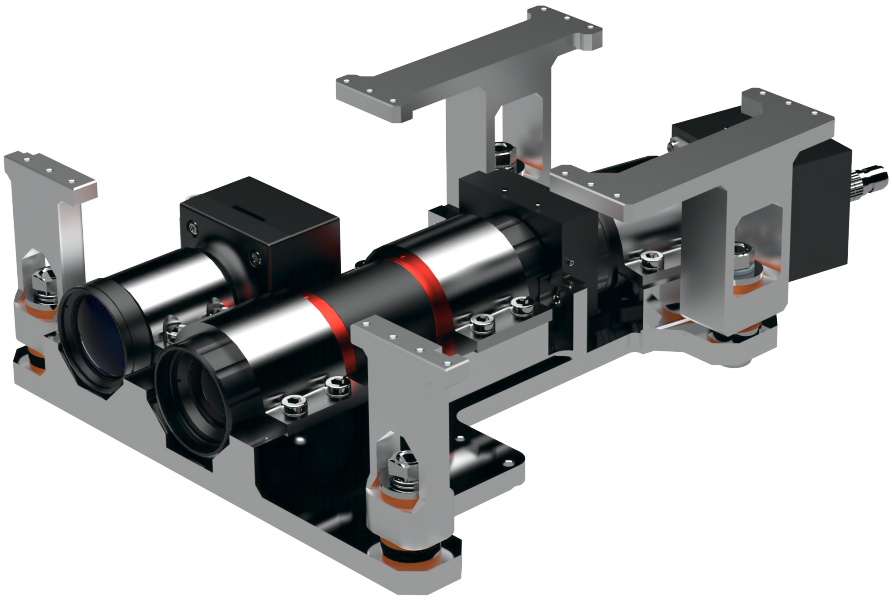

NTNU
Kunnskap for en bedre verden

Kristoffer Finnson
Fredrik Nes Fredheim
Andreas Inderberg

Simulation of Shock and Vibration Forces for Space-based Components

MTP-K-2021-04

Bachelor's project in Mechanical Engineering
Supervisor: Cecilia Haskins
Co-supervisor: Evelyn Honoré-Livermore
May 2021

Norwegian University of Science and Technology
Faculty of Engineering
Department of Mechanical and Industrial Engineering

NTNU

Kunnskap for en bedre verden

Abstract

The focus of this thesis is on shock and vibration simulations of a satellite as a part of the HYPSO project at NTNU. The purpose behind the work presented in this thesis is twofold: Firstly it is a way of exploring how shock and vibrations affect the satellite, and secondly it develops a method for setting up simulations that can be used and further developed by other satellite projects in the future.

The thesis describes the work process that led to the setup of simulations. This process started with idealization (simplification) of components that were to be simulated, and the removal of components that were considered less critical or too complicated for a simulation to be accurate. Then, finite element method (FEM) models were prepared by defining connections between the parts and determining simulation constraints and load scenarios. Simulations that replicate the conditions from physical tests were conducted, and comparisons between these simulation results and the corresponding test results were used to evaluate the accuracy of the simulation models.

After running several simulations, the results showed that the simulated models had higher resonance frequencies than the physical model, and also experienced higher peak response accelerations to shock and vibrations. We believe the main reasons for these differences are that the simulated models are stiffer than the real satellite, and that most simulations were performed without dampers. Towards the end of the project, a simulation model with dampers included was created, and their preliminary results showed promise, proving that dampers are necessary for simulations of the satellite to be realistic.

Sammendrag

Denne oppgaven handler om sjokk- og vibrasjons-simuleringer av en satellitt, som en del av HYPSO-prosjektet ved NTNU. Hensikten med arbeidet som blir presentert i denne oppgaven er todelt: For det første er det en måte å utforske hvordan sjokk og vibrasjoner påvirker satellitten, og for det andre utvikles en metode for å sette opp simuleringer, som kan bli brukt og videreutviklet av andre satellittprosjekter i fremtiden.

Oppgaven beskriver arbeidsprosessen som førte til oppsettet av simuleringer. Denne prosessen startet med idealisering (forenkling) av komponenter som skal simuleres, og fjerning av komponenter som blir ansett som mindre kritiske eller for kompliserte til at en simulering vil være nøyaktig. Deretter ble det satt opp en analyse ved hjelp av elementmetoden (FEM) ved å definere forbindelser mellom delene og bestemme begrensninger og laster for simuleringen. Det ble gjennomført simuleringer som gjenskaper forholdene under fysiske tester, og sammenligninger mellom disse simuleringsresultatene og de tilsvarende testresultatene ble brukt til å evaluere nøyaktigheten til simuleringsmodellen.

Etter å ha kjørt flere simuleringer, viste resultatene at den simulerte modellen har høyere resonansfrekvenser enn den fysiske modellen, i tillegg til at akselerasjonene ved sjokk og vibrasjoner var høyere. Hovedårsakene til disse forskjellene er sannsynligvis at den simulerte modellen er stivere enn den faktiske satellitten, og at de fleste simuleringene ble gjennomført uten dempere. Mot slutten av prosjektet ble det kjørt noen simuleringer med dempere, og de innledende resultatene virket lovende, noe som viser at dempere er nødvendige for at simuleringer av satellitten skal bli realistiske.

Preface

The work presented in this paper has been conducted at the Department of Mechanical and Industrial Engineering in collaboration with the Faculty of Information Technology and Electrical Engineering at NTNU, as part of the NTNU SmallSat program and the HYPSO project. This paper is authored by three engineering students, Andreas Inderberg, Fredrik Nes Fredheim and Kristoffer Finnson, under the supervision of Associate Professor Cecilia Haskins and co-supervision of Evelyn Honoré-Livermore.

We would like to thank the team members of HYPSO and NTNU SmallSat Lab for their support and advice throughout this project. A special thanks goes to Elizabeth Prentice and our project leader and co-supervisor Evelyn Honoré-Livermore for their exceptional assistance and guidance on both technical issues and on the writing of this thesis. We would also like to thank the HYPSO alumn Tuan Tran for helping us with the use of the computer software NX, and for his availability and willingness to provide assistance at any time.

Finally we thank our supervisor, Associate Professor Cecilia Haskins, for providing excellent guidance and inspiration during the whole process of writing this thesis. We are tremendously grateful for all her help, advice and feedback along the way.

Trondheim, May 20$^{\text{th}}$, 2021

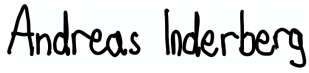
Andreas Inderberg


Fredrik Nes Fredheim


Kristoffer Finnson

Contents

List of Tables

List of Figures

Acronyms and Abbreviations

ADCS Attitude Determination and Control System

AUV Autonomous Underwater Vehicle

BoB Break-Out-Board

BRF Body Reference Frame

CAD Computer-Aided Design

CAE Computer-Aided Engineering

CoM Center of Mass

CONM2 Concentrated Mass Element

COTS Commercial Off-The-Shelf

CPU Central Processing Unit

DoF Degrees of Freedom

E-modulus Elastic Modulus

EM Engineering Model

EO Earth Observation

FEA Finite Element Analysis

FEM Finite Element Method

FFI Norwegian Defence Research Establishment

FM Flight Model

HSI Hyperspectral Imaging

HYPSO Hyper-Spectral SmallSat for Ocean Observation

IMU Inertial Measurement Unit

LEO Low Earth Orbit

MPE Maximum Predicted Environment

MTETT Minimum Two Elements Through Thickness

NIR Near Infrared

NTNU Norwegian University of Science and Technology

PSD Power Spectral Density

Q-factor Quality Factor

QM Qualification Model

RBE Rigid Body Element

RD Response Dynamics

RGB Red, Green and Blue

SDOF Single Degree of Freedom

SRS Shock Response Spectrum

SRSS Square Root of the Sum of the Squares

UAV Unmanned Aerial Vehicle

USV Unmanned Surface Vehicle

UTS Ultimate Strength

YS Yield Strength

Chapter 1

Introduction

1.1 HYPSO Project

The Hyper-Spectral SmallSat for Ocean Observation (HYPSO) is a science-oriented technology project at the Norwegian University of Science and Technology (NTNU), funded by the Norwegian Research Council. The HYPSO-team works in close cooperation with the Lithuanian aerospace engineering company NanoAvionics, who produces and delivers the satellite bus. The HYPSO project aims to launch a small satellite spacecraft known as a CubeSat into low earth orbit (LEO) to observe oceanographic phenomena. The satellite's payload, which is the HYPSO-team's main responsibility, consists of a hyperspectral imaging (HSI)-camera, a red, green and blue (RGB)-camera and electric components. There is also intelligent on-board processing that compresses the data and provides the data products end-users want for downlinking to Earth. The HSI-camera will be calibrated for detection of algae and phytoplankton. This information can be communicated to autonomous assets with similar objectives, such as unmanned aerial vehicles (UAVs), unmanned surface vehicles (USVs), autonomous underwater vehicles (AUVs) or buoys, which can then perform further investigations on the areas of interest and support expert analysis to determine whether the algae are harmful. The information gathered by the spacecraft can also be useful for understanding more about the effects of climate change and human impact on the planet [1].

This spacecraft will be able to conduct high-performance hyperspectral imaging and autonomous onboard processing at a relatively low cost. This is achieved by producing a payload component using commercial off-the-shelf (COTS) parts, which are cheaper than their space-graded alternatives. One reason for the added cost is that space-graded components require a lot of documentation to prove their space grade authenticity. The intention of this project is to provide evidence that the commercial parts will also be able to survive launch and harsh space environments.

The HYPSO-team consists of master and bachelor students, PHD candidates and supporting professors. The team is divided into specialized subsections including software, hardware, attitude determination and control system (ADCS) and on-board processing. The head of the organization is project manager Evelyn Honoré-Livermore. The payload development is supported by the NTNU SmallSat Lab within the Department of Engineering Cybernetics and Department of Electronic Systems.

1.2 Problem Description

For the satellite to fulfill its mission, it is vital that the components do not suffer any significant damage from the exposure to shock and vibrations during launch. In order to understand how the satellite and its payload react to these loads, various tests and simulations can be conducted. Physical tests are always the most accurate, given working sensors. Simulations however are very attractive because of their convenience. They require little resources and the results are usually ready within hours. This is opposed to physical tests that require a lot of preparation and work. Figure 1.1 shows a mechanical test setup of HYPSO-1 with sensors attached.

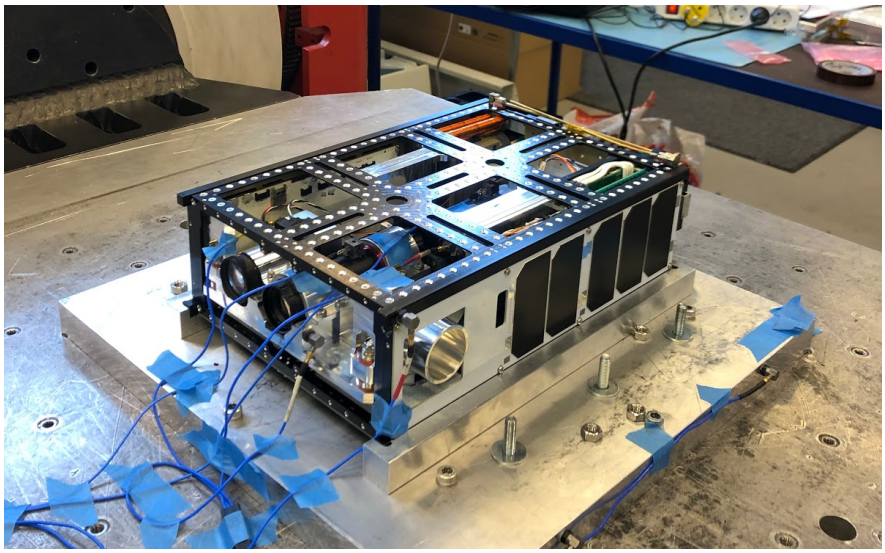

Figure 1.1: HYPSO-1 mechanical test setup [2]

This thesis will focus on creating simulations to study the satellite's reaction to different shock and vibrational loads. These loads will be defined from the requirements set by SpaceX and our partner NanoAvionics. Before the work with this thesis began, several physical tests of shock and vibration forces had already been performed by the mechanical team of the HYPSO-project. The simulations will also replicate these test conditions, so we can compare the results from the simulation and the physical tests. This comparison will be useful for verifying the quality of the simulation model. The purposes of making these simulations are to identify critical components and connections that may be prone to failure, and to create a simulation blueprint that the HYPSO-team can use to improve the design of the second generation CubeSat, HYPSO-2.

Chapter 2

Background and Theory

This chapter will provide relevant information needed to follow and understand this thesis. We first give an introduction to some of the challenges related to the environment in space. Then we describe the satellite and how it works. Following this, we explain how shock and vibration loads affect the satellite, and why these loads are important to study.

2.1 The Space Environment

When designing a spacecraft, it is important to consider the environmental conditions in space, which are different from the conditions on Earth. For instance, the lack of protection from an atmosphere increases the hazard of ionizing radiation, which affects delicate electronics unless they are properly shielded [3]. Furthermore, the spacecraft must be able to operate in vacuum conditions with extreme temperature fluctuations. In a vacuum, there is a risk of materials being subject to outgassing, which means that volatile substances are released from the surface of the material. If this happens, the outgassed matter may contaminate equipment such as solar arrays or optics [4]. Another risk to satellites is the increasing amount of orbital debris. Natural micrometeoroids and man-made debris, such as remnants from previous space missions are orbiting the Earth at speeds of approximately 10 km/s. Due to the high velocities, any impact with a satellite is likely to cause considerable damage,

irrespective of the size of the debris [5]. These are all conditions that the spacecraft will experience in orbit, but this thesis will focus primarily on the challenging conditions at launch: namely shock, resonance and vibrations.

2.2 SmallSats

A SmallSat is a spacecraft with a lower mass than 180 kilograms. Within the SmallSat-category there are several variants that are differentiated by the spacecraft's mass [6]. The HYPSO-satellite, HYPSO-1, is a nanosatellite with a total mass of roughly 6.5 kg. The different variants of small satellites are shown in table 2.1.

Table 2.1: Classifications of SmallSats [7]

SmallSat Type	**Weight [kg]**
Minisatellites	100 - 180
Microsatellites	10 - 100
Nanosatellites	1 - 10
Picosatellites	0.01 - 1
Femtosatellites	less than 0.01

Over the years, many of the launched satellites would fall under the classification SmallSat, so this is nothing new. The difference however, and what makes the HYPSO-1 spacecraft and other modern SmallSats interesting, is the use of modular COTS-components. This gives modern SmallSats a big advantage over traditional earth observation (EO) satellites, reducing the time and cost of development [8], [9]. The cost of deployment is also greatly reduced as the spacecraft can rideshare on a rocket with free space.

Another characteristic of SmallSats is shorter operational lifetimes, due to the fact that they are being launched into LEO, meaning they will drop down to earth earlier. This means that they have to be developed and launched more frequently. The life cycle can however be adjusted to be compatible with technological upgrades [9]. Some CubeSats have

also been in operation for nearly 10 years [10]. The reduced lifetime of SmallSats could also put strain on an existing big problem for the space sector, space debris. Launching SmallSats into space more frequently without any plan for decommissioning them will inevitably lead to a lot of dead satellites in orbit [11], luckily SmallSats today must have such a plan before they are cleared for launch [12]. It is also common for waiting times associated with piggyback or rideshare launches to be significant.

CubeSats

A CubeSat is a type of nanosatellite that uses a standard size and shape factor. The standard CubeSat size is called "one unit" (1U), and is a cube of 10x10x10 cm. Larger CubeSats consist of more units and are labeled accordingly [6]. For example, 2U consists of two units, 3U has three-, and 6U has six units. This concept is illustrated in Figure 2.1. The HYPSO-1 spacecraft is using a 6U-CubeSat size.

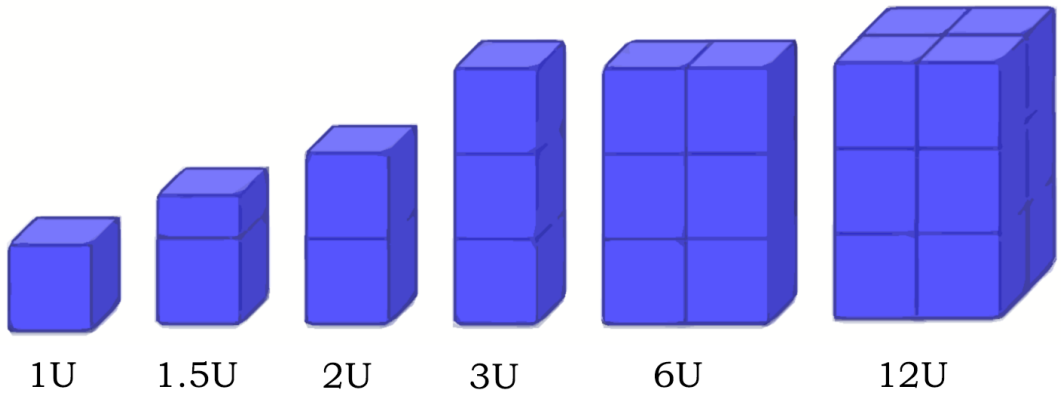

Figure 2.1: Unit-configurations for CubeSats of various sizes [7]

2.3 Payload

Since NTNU SmallSat Lab is only responsible for the satellites payload, this is going to be the focus of our analysis. It consists of a HSI-camera, RGB-camera and mechanical supports, which can be seen in figure 2.2. It also includes some electronic components for controlling the payload, which we will not be looking at in this study. It is particularly important when simulating shock and vibrational forces to look at the payload parts that are related to the

hyperspectral imaging (i.e. the HSI-camera's components.) This is because those parts of the payload are critical for the execution of the mission, and many of the parts are sensitive COTS-components.

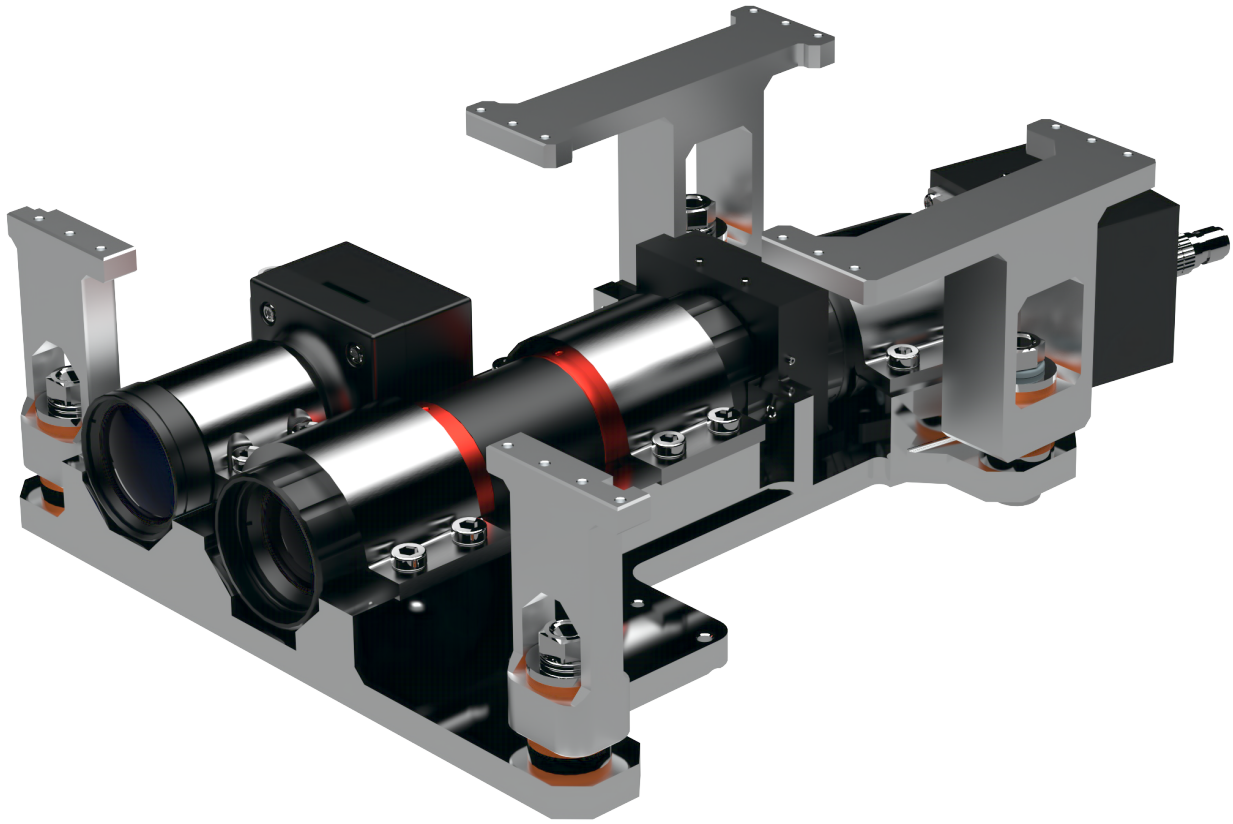

Figure 2.2: Rendering of the payload

2.3.1 Hyperspectral Imaging Camera

The HSI-camera (seen in figure 2.3) in the HYPSO-satellite is an assembly consisting of COTS-components and parts that are designed in-house. The COTS-components are the lens objectives, slit, grating and detector. The slit tube, detector housing and cassette for the grating are all designed at NTNU. In HYPSO-1 the HSI-camera is located such that the front objective is in the middle of the front face of the satellite. It is mounted to the HSI-platform with brackets that are screwed in place.

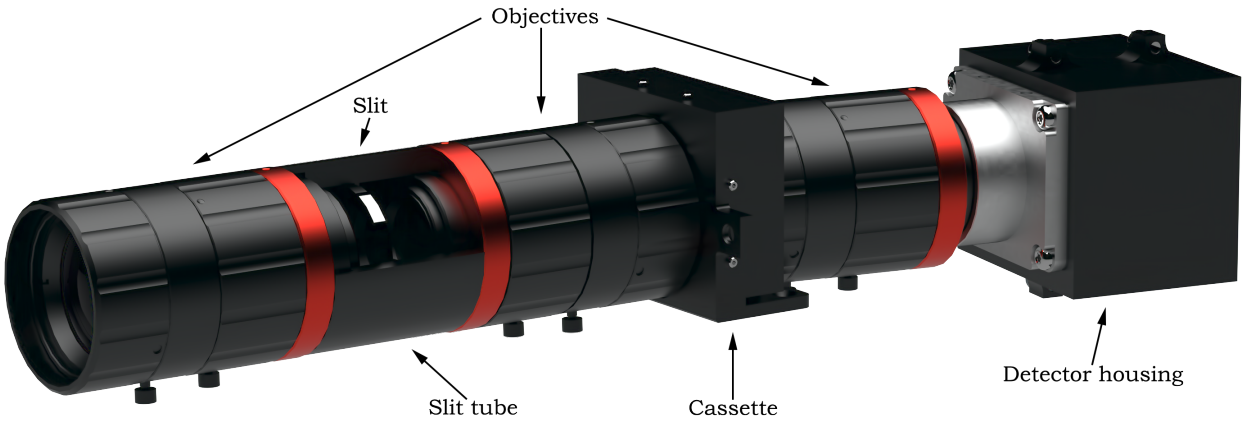

Figure 2.3: Rendering of the HSI-camera

A HSI-camera has the ability to capture a continuous color spectrum in the visible to near infrared (NIR) wavelengths, while the RGB-camera can only give information in the three red-green-blue wavelength channels. These wavelengths are captured as a three-dimensional dataset of spatial and spectral information, known as a hypercube [13]. By visualizing the electromagnetic spectrum, a hyperspectral camera can be used to precisely identify specific material signatures [14], [15]. In the case of HYPSO, the HSI-camera will take highly detailed images of the ocean and marine life using the pushbroom method. Figure 2.4 shows a hyperspectral image versus a RGB image.

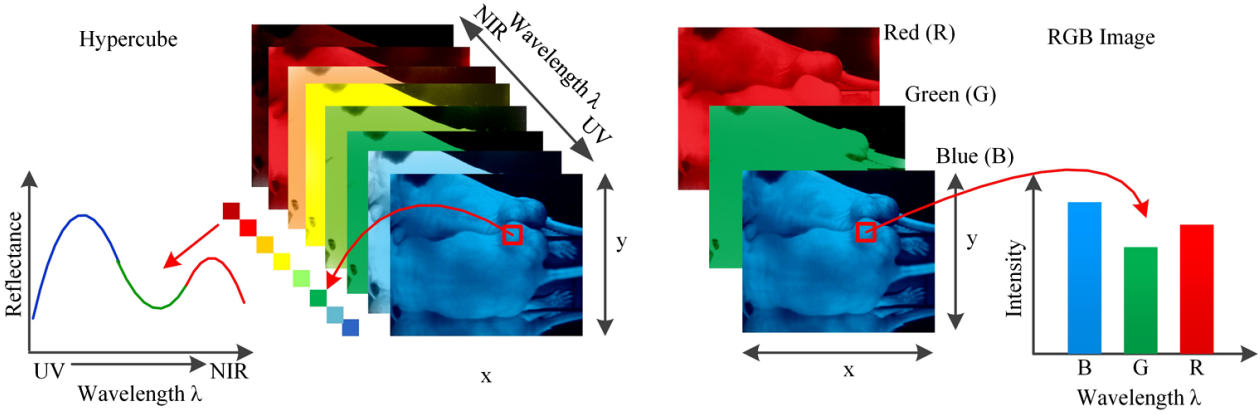

Figure 2.4: Comparison between a hypercube and RGB image. The lower left is the spectral signature of a pixel in the HSI image. The lower right is the intensity curve of a pixel in the RGB image [13]

Pushbroom

For EO satellites there are two main methods for passive optical imaging: whisk broom and pushbroom. These both collect images of the surface in long narrow strips perpendicular to the flight direction, called swaths. Whisk broom sweeps across the swath, collecting data one pixel at the time. This requires a lot of fast moving parts, which are more likely to break [16]. The pushbroom method on the other hand, scans the entire swath at once, building the image one narrow line at the time [17]. Most EO-satellites carry a pushbroom based payload today.

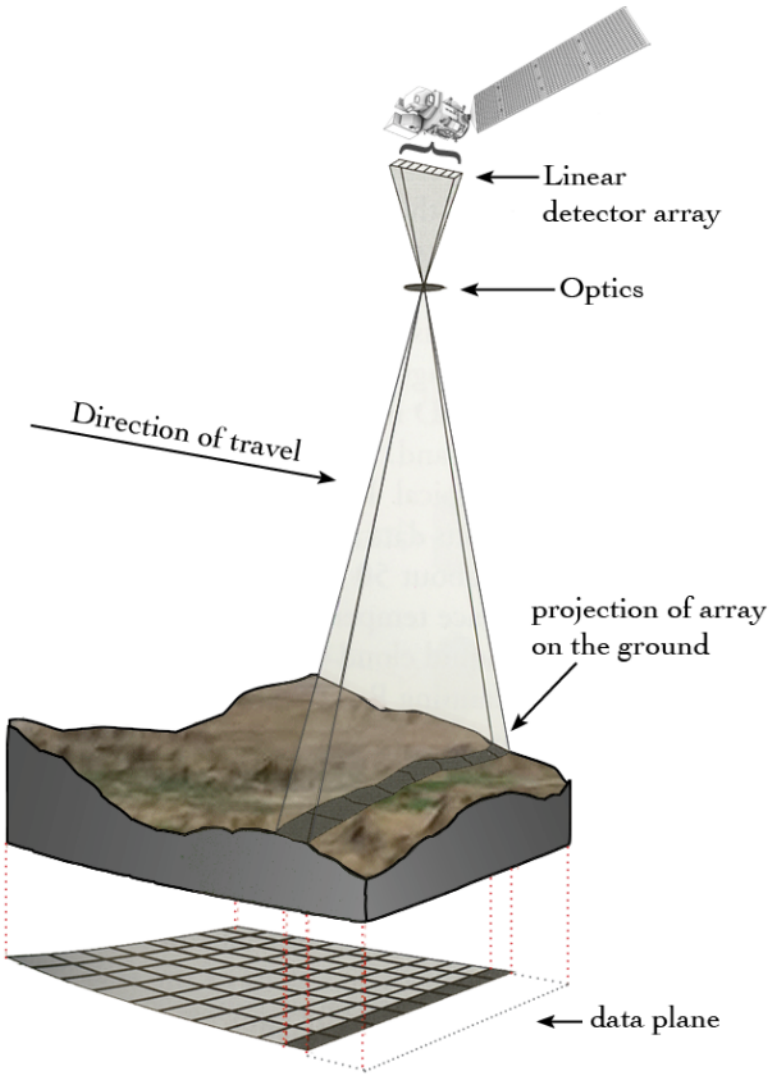

Figure 2.5: The pushbroom method [16]

2.3.2 RGB-Camera

A RGB-camera is included in the HYPSO-payload to provide pictures of the earth that can be used for georeferencing. It is located next to the HSI-camera on the HSI-platform, and is held in place by a bracket that is screwed to the platform. The RGB-camera consists of several COTS-components: the detector, objective lens and a C-mount for attaching the lens. It also has a housing part that assembles to the back of the C-mount, this part is designed at NTNU.

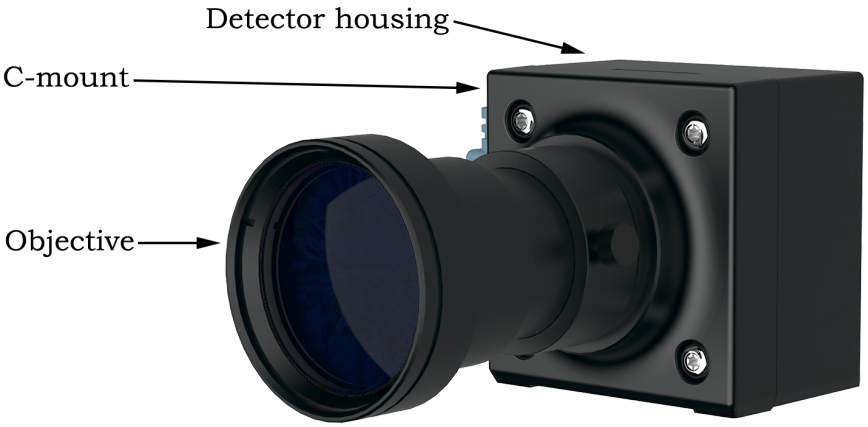

Figure 2.6: Rendering of the RGB-camera

Georeferencing

When HYPSO has detected important information such as harmful algae blooms, georeferencing is necessary to locate the area of interest as precisely as possible. In the process of georeferencing, images from the RGB camera are processed by an algorithm to determine the coordinates on earth [18]. This is useful for transmitting accurate information about the location of algae blooms to UAVs, USVs and AUVs. Figure 2.7 shows the georeferencing process. In order to achieve accurate georeferencing, the RGB camera is rigidly attached to the HSI, so that the cameras can be calibrated together prior to the mission. The difficulty of the georeferencing process would increase if the cameras change positions relative to each other during vibrations at launch, which is another reason why vibration studies of the satellite are important.

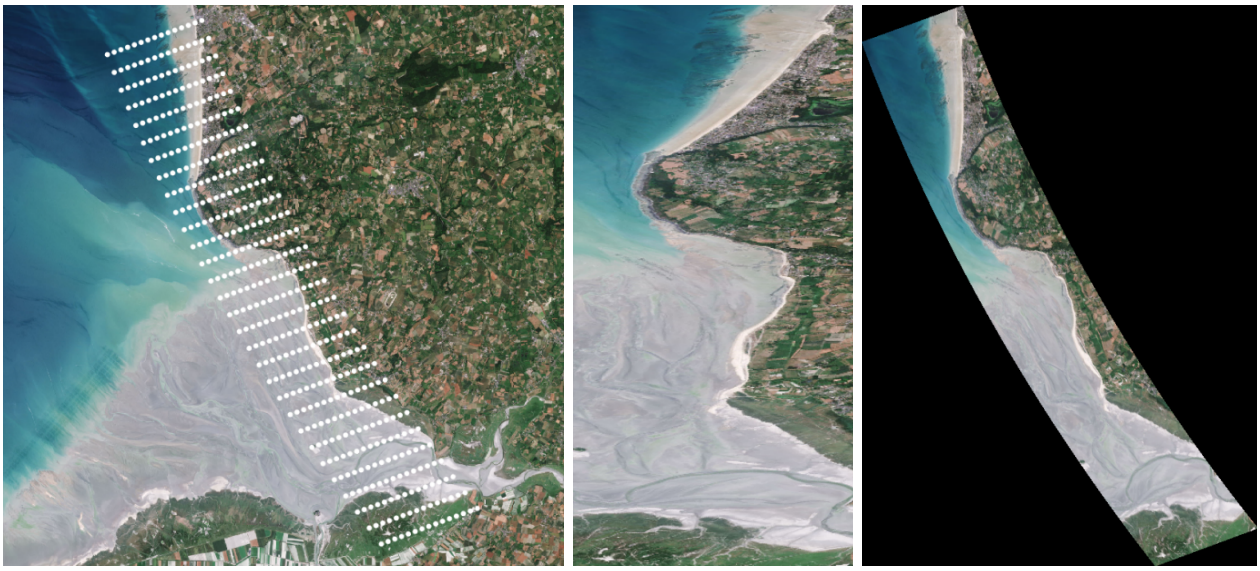

Ground picture Raw image Registered and georeferenced

Figure 2.7: Georeferencing process [18]

2.4 Challenges at Launch

2.4.1 Vibration

Mechanical vibration is a phenomenon where oscillations occur about an equilibrium point. Vibrations in mechanical structures are typically unwanted, and can cause structural and electrical failure. Therefore, satellites must undergo rigorous testing to check if they can survive various levels of vibration expected throughout their mission. Vibration tests can identify loose components and overall integrity of a CubeSat structure. Analysis of vibration is necessary in order to optimize the dynamic performance of a CubeSat and avoid that the natural frequencies are amplified by the vibration levels of a launch vehicle [19].

2.4.2 Random Vibration

When analyzing vibrations, one usually attempts to characterize the data as simply as possible. If for example the frequency and amplitude are constant, the vibration can be illustrated sinusoidally. However, if the vibrations do not follow any continuous pattern or regularity, they are called random vibrations. An example of this is shown in figure 2.8. Random vibra-

tions cannot be illustrated in a simple manner, and the parameters are unpredictable, due to fluctuations in variables that cannot be controlled. Therefore, a statistical description is more meaningful [20].

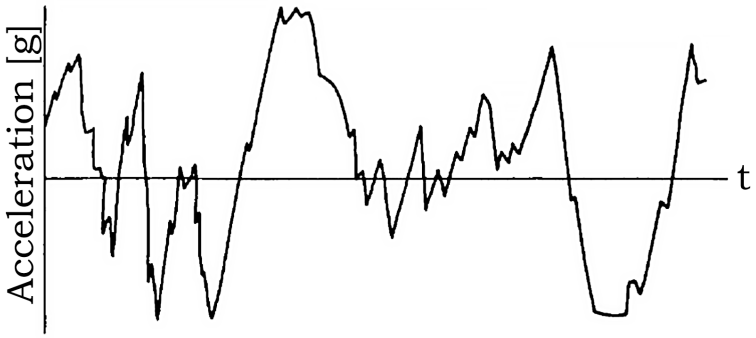

Figure 2.8: An example of random vibration [20]

Random vibration is defined as motion which is non-deterministic, meaning that future behaviour cannot be precisely predicted. Random frequencies are considered to replicate real world environments that may be encountered during the life span of a mechanical structure. The power spectral density (PSD) is commonly used to specify a random vibration event. The PSD of a signal gives an analysis of the distribution of power over the entire frequency range.

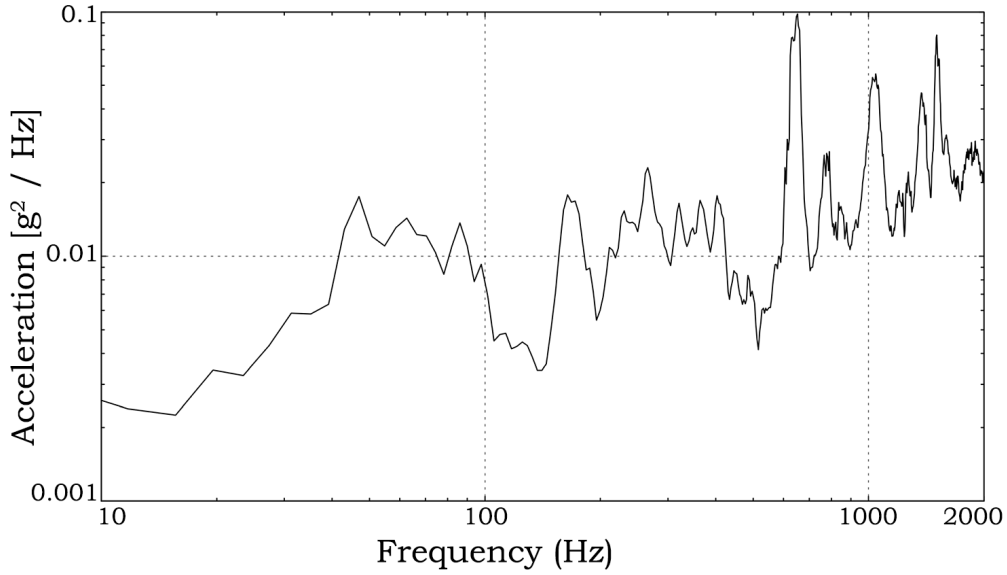

Figure 2.9: An example of power spectral density [21]

For the HYPSO spacecraft, the random vibration maximum predicted environment (MPE), with the corresponding PSD, is found in table 5.4. The MPE is an envelope of all flight events (liftoff, first stage ascent, and second stage burns) [22]. Random vibrations are caused by flight environments that generate dynamic loads occurring in combinations and at various times during flight. The flight environments divide into three main categories [23]:

1. Low-frequency dynamic response
    - 0 Hz to 50 Hz
    - Of the launch vehicle/payload system to transient flight events
2. High frequency random vibration
    - 20 Hz to 2000 Hz
    - Transmitted from the launch vehicle to the payload at the launch vehicle/payload interfaces
3. High frequency acoustic pressure environment
    - 31 Hz to 10,000 Hz
    - Occurs inside the payload compartment
    - Generated by direct impingement on the surfaces of exposed components
    - Also generated by the acoustic pressure impingement upon the component mounting structures, which induces random vibrations that are mechanically transmitted to the components

2.4.3 Resonance

Resonance happens when the forcing frequency acting on an oscillating system equals the natural frequency of the very same system. An example explaining this concept could be a child on a swing. For the child to be pushed higher, we need to push with the same oscillating frequency as the swing has — at specific time intervals [24].

Natural frequencies, or eigenfrequencies are defined as the frequency at which a system tends to oscillate in the absence of any driving or damping force [25]. Eigenfrequencies describe the ratio between stiffness and mass. A system oscillating at its natural frequency is described by a normal mode.

A modal analysis is used to determine the dynamic characteristics (natural frequencies and mode shapes) of mechanical structures and components [26]. If a component is subject to vibrations or periodically applied forces at a frequency that is equal or close to the natural frequency, resonance will occur. This causes high amplitude vibrations and dynamic stresses, which potentially can produce significant damage to the components involved [27]. Therefore, the natural frequency is an important parameter in the design of any structure that will be exposed to dynamic loading conditions.

Resonant frequencies must be restricted to particular bandwidths. These specified bandwidths have been selected in order to prevent dynamic coupling with major excitation frequencies (fundamental frequencies of the launch vehicle) [28]. We also have to keep in mind that the resonance conditions must be evaluated on a case by case basis. Generally the higher the frequency the lower the risk of damage. This is due to displacement being inversely proportional to the square of the frequency [29].

2.4.4 Shock

Mechanical or physical shock is defined as a transient physical excitation where a sudden acceleration is caused. The impulse can come from drop, kick, impact, or explosion. Shock describes matter subject to extreme rates of force with respect to time. Shock is a vector measured in g , which represents acceleration (change of velocity). One g is equal to the acceleration of gravity at $9.80665\ \frac{m}{s^2}$ [30].

Shock pulses can occur on the satellite during transportation, launch/separation stages, and from space environments. They are characterized by their duration, peak acceleration, and shape (half sine, square, trapezoidal, etc.). Consider a transportation container placed on a truck that runs over a speed bump. The payload components inside may experience a half sine pulse. This type of pulse can be represented in the time domain by its duration and peak amplitude. Figure 2.10 shows a half sine pulse, and figure 2.11 shows the corresponding shock response spectrum.

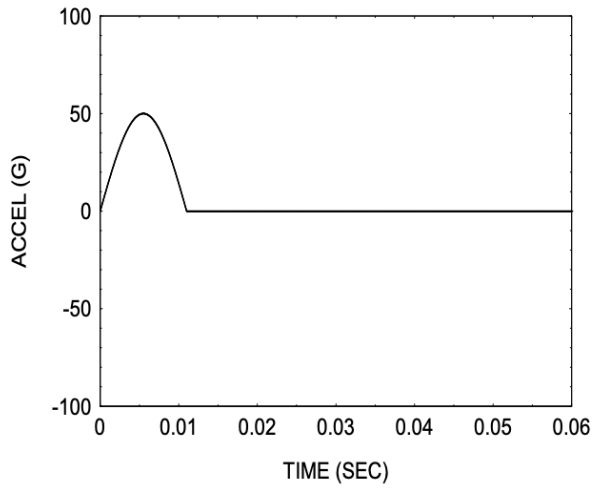

Figure 2.10: Half sine pulse [31]

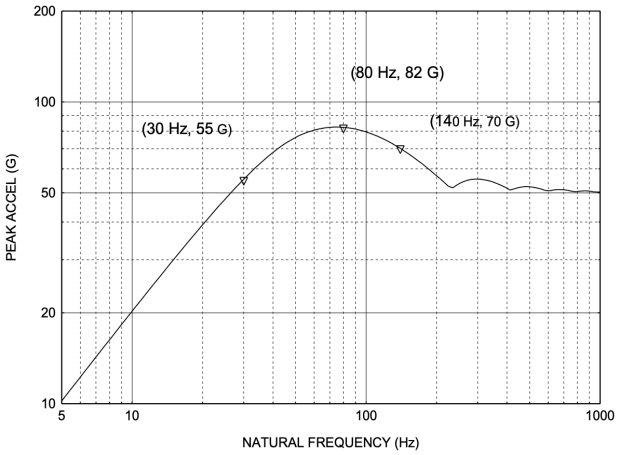

Figure 2.11: Shock response spectrum of the half sine pulse [31]

The shock response spectrum (SRS) is a method for evaluating a mechanical shock, and describes how a single degree of freedom (SDOF) system responds to a transient acceleration input. In aerospace industry, the dimensions in the SRS are typically natural frequency of a SDOF on the x-axis, and the peak acceleration this SDOF would undergo from the shock input on the y-axis. The SRS is a helpful tool for estimating the damage potential of a shock pulse. It is a calculated function based on the acceleration time history as a base excitation to an array of SDOF systems. The damping of the SDOF system is typically assumed as 5%, which is equivalent to a quality factor (Q-factor) of 10.

The HYPSO spacecraft will experience several shock pulses during the launch sequence. Various shock loads imposed from the Falcon 9 rocket during launch are results from the following events [28]:

- Release of the Launch Vehicle hold-down during liftoff
- Booster and second stage separation
- Fairing deployment
- Co-nanosatellite separation(s)
- Nanosatellite separation

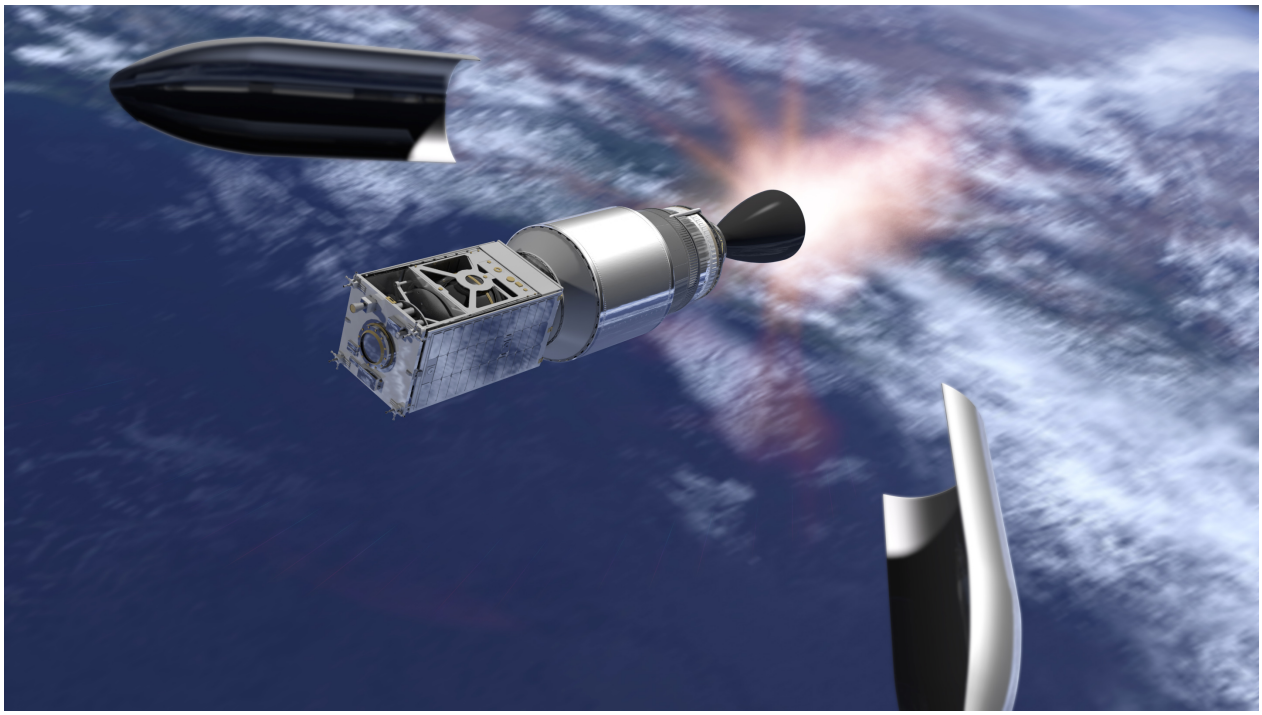

Figure 2.12: Fairing deployment [32]

The first two events; release of the Launch Vehicle hold-down during liftoff and the booster and second stage separation, are not taken into account for shock as these are negligible for the nanosatellites when compared to the other three events listed above. The shock MPE for fairing deployment and co-nanosatellite separation(s) are defined in table 5.6.

2.5 Degrees of Freedom

In mechanics, the degrees of freedom (DoF) refer to a solid object's ability to change its position and/or orientation. In three dimensional space, a rigid body has six DoF: Its position can change through translational motion along the x-, y- and z-axis (left/right, forwards/backward and up/down), and its orientation can change by rotating around the x-, y- and z-axis.

When making a 3D simulation, it is often necessary to define constraints for one or more of the simulated object's DoF. This depends on the way the object is mounted to its surrounding parts.

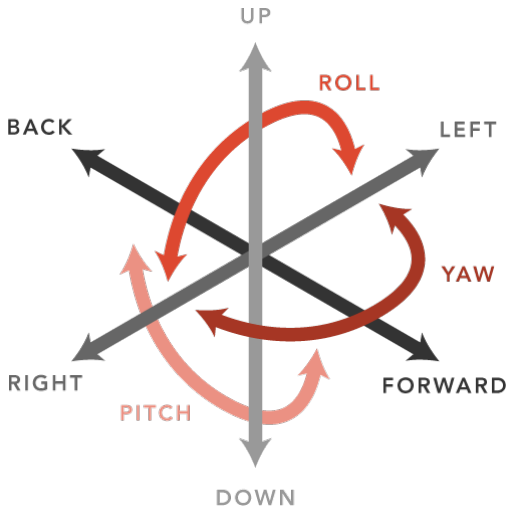

Figure 2.13: Illustration of the six degrees of freedom [33]

Chapter 3

Method and Tools

This chapter gives an overview of the work procedure and the tools we used during this project.

3.1 Method

3.1.1 Document Reuse and Review

Setting up simulations for complex structures such as the HYPSO-1 spacecraft requires a lot of information. Not only for the simulation itself but also for the people creating it. At the beginning of our project, it was necessary to do a literature review on shock and vibrations, in order to acquire enough background information and knowledge to get started. When searching for information, we mainly used the online academic databases Scopus and Google Scholar, with keywords such as "mechanical", "shock", "vibration", "fem", and "analysis". The results of our literature review combined with documents shared by the HYPSO-team, were important for gathering fundamental knowledge to make the simulations reliable. The documents were read mostly before the spring semester, but have been a huge help going back to and reviewing at later stages when we needed to find certain information.

The HYPSO-team uses the cloud storage service, Google Drive, to store all their engineering literature and documents. Since the project has been ongoing for about 3 years [34] at this time, and every member of the team stores their work here, the library naturally has grown very large. During the beginning of the project we had to find a lot of information in this library, such as materials, weight and coordinates of the components currently on the satellite. Knowing how to search this library for relevant literature and information effectively, was therefore crucial for maintaining a steady progression on the project. In order to find the correct information, we familiarized ourselves with the folder structure in Google Drive and received recommendations from team-members for relevant documents. The documents we found to be the most relevant and helpful for our assignment are shown in table 3.1.

Table 3.1: Relevant documents

Document ID	**Author(s)**	**Title**
HYPSO-TRP-VIB-003	M. Hjertenæs, E. Prentice, T. Kaasa	Shock, Resonance, and Vibration of CLAW-1 - QM
HYPSO-TRP-VIB-002	M. Hjertenæs, E. Prentice, T. Kaasa	Shock, Resonance, and Vibration of CLAW-1 - EM
HYPSO-ANA-009	T. Tran, T. Kaasa	HSI Payload Mechanical Analysis Report

3.1.2 Work Structure and Development

We split this project into two phases. The first phase consisted of gathering all the information needed to set up a simulation, and prepare the computer-aided design (CAD) components (see figure 3.1). The second phase was the construction and analysis of the simulations. For the first phase, one of the first things we did was create a spreadsheet (see appendix B) to get an overview of all the components in the satellite. We made it clear what components were to be idealized, turned to point masses, or removed. We also listed all the materials for the idealized components, and found the mass and coordinates for the point masses.

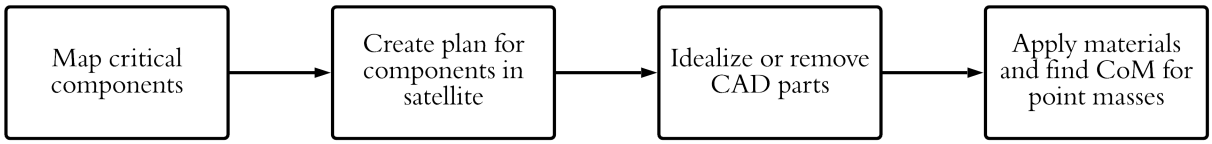

Figure 3.1: Planning and CAD phase

For the second phase (see figure 3.2) we first had to construct the finite element method (FEM) file that the simulations are based on. This process included applying materials, defining connections and point masses, and creating mesh for every single idealized part. To make sure our model was accurate, we ran mesh convergence studies that helped us locate areas that needed refinement. In order to run the simulations we had to figure out what solvers to use (see section 5.1) and what the input values should be. Our plan was to run simple simulations in the beginning, then incrementally add complexity. This part of the plan changed over time, and instead we created three different models with different levels of complexity. We did however refine the models slightly, after running some preliminary simulations. When all this was done we put the models through multiple simulations based on previously executed physical tests. Results from these were then compared to the physical results from the qualification model (QM). After comparing and seeing the differences in results, we ran the Falcon 9 shock test that the physical drop table was not able to perform.

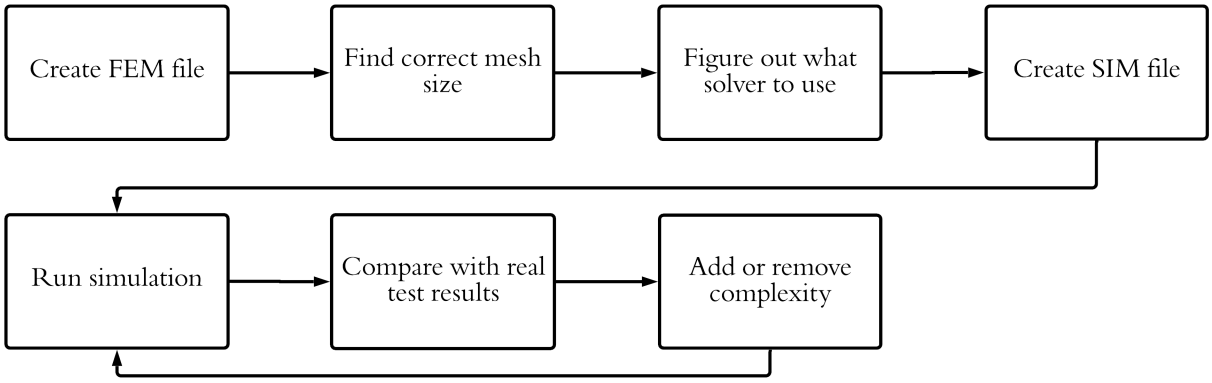

Figure 3.2: Simulation creation and execution phase

3.2 Software Tools

CAD is the use of software to aid the engineering process of creation, modification, analysis, or optimization of components and products. These programs store relevant information about the parts such as materials, dimensions, mass, and creation history, which is useful if it becomes necessary to modify a part.

At the beginning of the project it was important to choose the right CAD and computer-aided engineering (CAE) tools. NTNU coursework offers experience using SolidWorks, which is a CAD and CAE tool by Dassault Systèmes, and we were comfortable with our abilities in this program. HYPSO on the other hand uses Siemens NX, a tool we had not used before. This meant that if we were to use NX we would have to learn a completely new CAD tool. If we were to choose SolidWorks we would have to convert all the part files currently in NX to files that SolidWorks could read. NX also has a finite element analysis (FEA) tool called Nastran, which can simulate shock and vibrations and has a solid reputation. Therefore, we concluded that using NX and NX Nastran was the better alternative.

Chapter 4

Finite Element Model

In this chapter we explain what FEM is and our approach to creating one. This includes simplifying the components (idealization), choosing the right mesh element sizes, and defining connections. We also give an overview of the components in our models.

4.1 Finite Element Analysis

The finite element method (FEM) is a numerical technique used to perform finite element analysis (FEA) on different engineering and mathematical problems. To solve these problems the simulation program divides a larger part into a finite amount of smaller, simpler shapes or elements called finite elements. This allows the simulation program to analyze the elements with mathematical formulas defined in its different solvers, and determine the behaviour of the larger part as a whole. The results acquired from the analysis can also be displayed visually on the part to better understand them. This whole process is exemplified in figure 4.1.

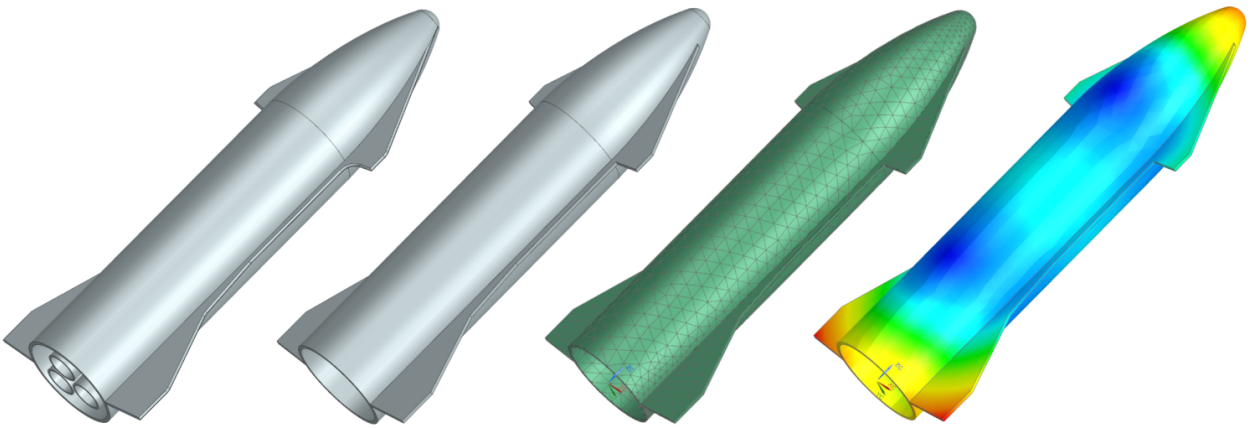

Figure 4.1: Process of creating a finite element analysis of a dummy Starship. From left to right: original, idealized, meshed, results

4.2 Satellite Overview

This section will give an overview of all the relevant parts the satellite consists of. We believe that, due to the complexity caused by the large number of parts, having this overview is helpful in following the thesis further. We have divided the satellite assembly into six smaller subassemblies for our models, and it is this arrangement that is used below. Material properties are given in section 4.3.

NX Assembly

The reference frame we will be using is one we will be calling the body reference frame (BRF). This is a coordinate system with three mutually perpendicular axes that has its origin in the center point of the satellite frame. Figure 4.2 shows our model and its BRF.

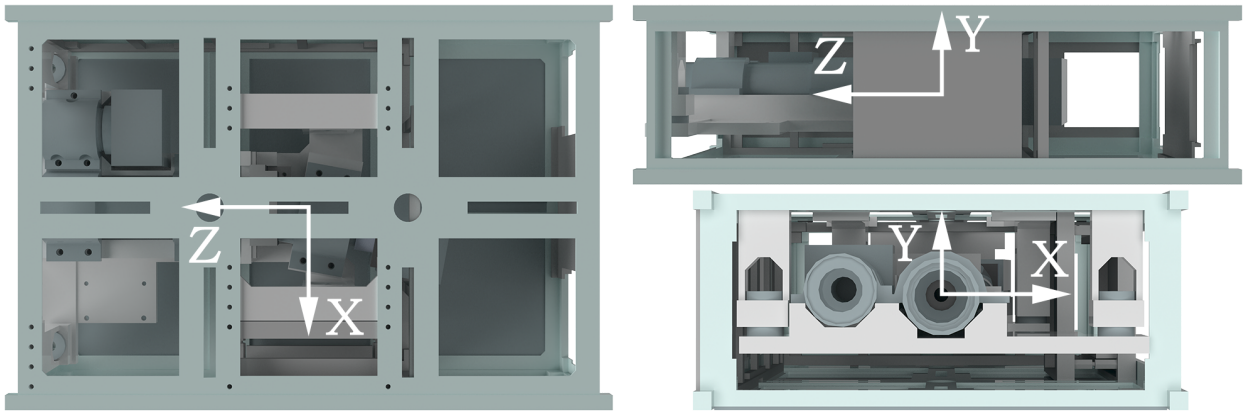

Figure 4.2: Idealized model with the body reference frame

The HSI Platform

This is the platform that the HSI- and RGB-camera, and the inertial measurement unit (IMU) and star tracker are mounted to. Four crosslinks together with eight dampers connect the platform to the frame.

Table 4.1: Overview of the components in the platform sub-assembly

HSI Platform			
Component	**Qty**	**Change**	**Material**
Platform	1	Idealized	AA 6082-T6
Front crosslinks	2	Idealized	AA 6082-T6
Back crosslinks	2	Idealized	AA 6082-T6
Dampers	8	CBUSH	SMACSIL
Star tracker	1	Point mass	-
IMU	1	Point mass	-

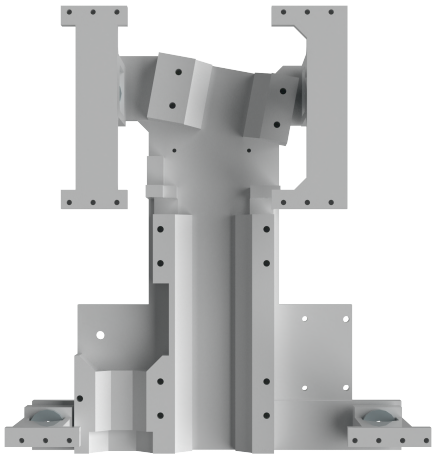

Figure 4.3: The platform assembly

The Frame

The frame model consists of the satellite's framework and solar panels, which make up the external structure of the spacecraft. Here we also find the communication equipment, electronics, ADCS devices, and picoBoB. Most of the components in this model will be produced by NanoAvionics. The parts we considered important for structural stiffness were idealized, and the rest were made point masses.

Table 4.2: Overview of the components in the frame subassembly

Frame			
Component	**Qty**	**Change**	**Material**
6U Frame	1	Idealized	AA 7075-T7
3U Ring frame	1	Idealized	AA 7075-T7
2U Ring frame	1	Idealized	AA 7075-T7
PicoBoB	1	Idealized	AA 6082-T6
Tuna can	2	Point mass	-
Magnetorquer	6	Point mass	-
Electronics stack	1	Point mass	-
Payload controler	1	Point mass	-
Reaction wheels	4	Point mass	-
SBand plate	1	Idealized	AA 7075-T7
SBand radio	1	Point mass	-
Solar panels	4	Idealized	FR4

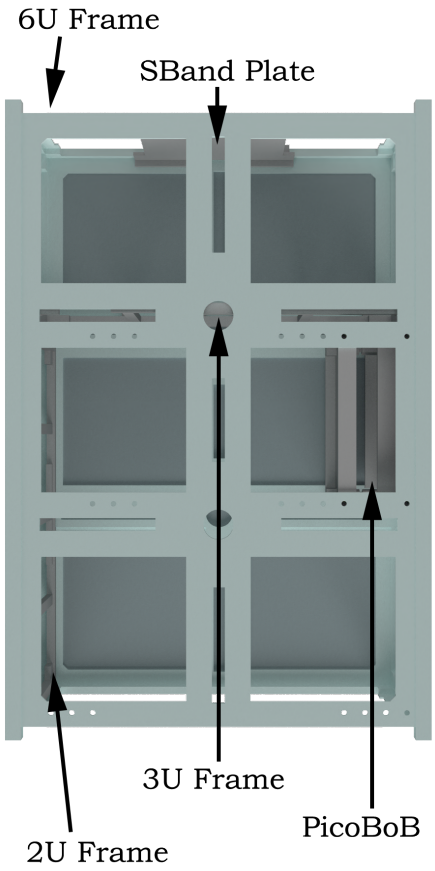

Figure 4.4: The frame assembly, with the top solar panel hidden

The Front Payload

This includes the RGB camera and the front and middle objectives of the HSI, as well as the HSI's slit and slit tube. As mentioned in sections 2.3.1 and 2.3.2, the cameras are fastened with brackets that are bolted to the platform.

Table 4.3: Overview of the components in the front payload subassembly

Payload Front			
Component	**Qty**	**Change**	**Material**
RGB objective	1	Idealize	AA 6061-T6
RGB detector	1	Point mass	-
RGB detector housing	1	Idealize	AA 6082-T6
Brackets	3	Idealize	AA 6082-T6
HSI objectives	2	Idealize	AA 6061-T6
Slit	1	Idealize	AA 6061-T6
Slit tube	1	Idealize	AA 6082-T6

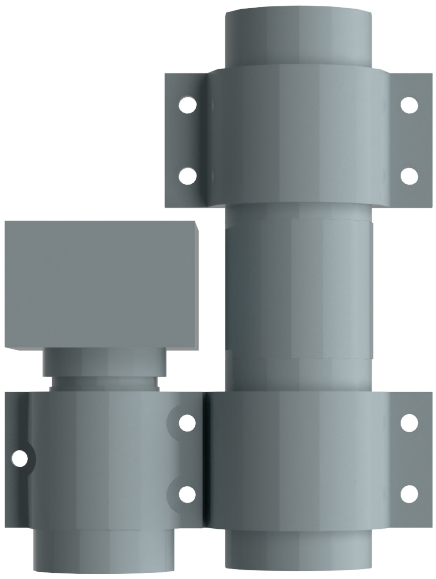

Figure 4.5: The front payload assembly

The Rear Payload

These are the parts of the HSI-camera that are located behind the cassette, i.e. the rear objective, the detector, the detector housing and a platform bracket.

Table 4.4: Overview of the components in the rear payload subassembly

Payload Rear			
Component	**Qty**	**Change**	**Material**
HSI objective	1	Idealize	AA 6061-T6
HSI detector	1	Point mass	-
HSI detector housing	1	Idealize	AA 6082-T6
Bracket	1	Idealize	AA 6082-T6

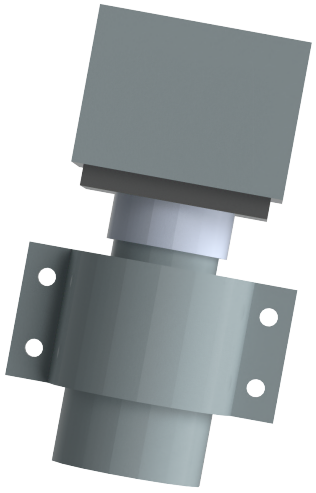

Figure 4.6: The rear payload assembly

The Cassette

The cassette houses the grating and some brackets to hold it in place. The grating is a fragile piece of glass and is a part of the HSI optics [35]. Including the grating in our simulations would add unnecessary complexity, and was therefore made a point mass.

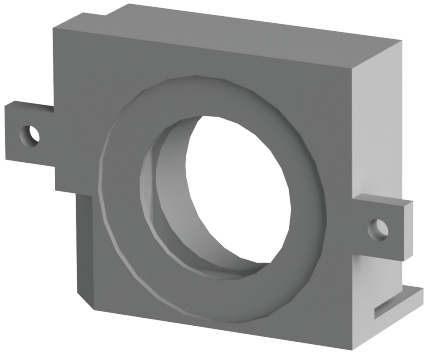

Figure 4.7: The cassette assembly

Table 4.5: Overview of the components in the cassette subassembly

Cassette			
Component	**Qty**	**Change**	**Material**
Cassette front	1	Idealize	AA 6082-T6
Cassette back	1	Idealize	AA 6082-T6
Grating	1	Point mass	-

4.3 Materials and Weight

Table 4.6 gives an overview of the properties: yield strength (YS), ultimate strength (UTS), elastic modulus (E-modulus) and density for the materials included in the idealized model of HYPSO-1. The damper material SMACSIL is not listed here as we were unable to find its material properties, luckily they were not needed. See section 4.6.4 for more information about the material.

Table 4.6: Material properties

Material	**Density [g/cm^3]**	**E-Modulus [GPa]**	**UTS [MPa]**	**YS [MPa]**
AA 7075-T7	2.81	72.00	462.00	386.00
AA 6082-T6	2.70	71.92	310.00	259.23
AA 6061-T6	2.70	68.90	310.00	276.00
FR4	2.00	21.56	240.00	240.00

The total mass of our simulated satellite model is 6574 grams. This is within the estimated weight that HYPSO believes the satellite will have, which is 6 671 $\pm$ 132 grams. Our model is towards the lighter side, which makes it stiffer. This is something we should keep in mind.

4.4 Idealization

If we were to run a simulation with all the parts unchanged, the time it would take to solve would be unnecessarily high. This is because more geometrical complexity requires more mesh elements, which means the central processing unit (CPU) has to conduct more calculations. Most of these complexities in the geometry have little to no impact on the results of the simulations, and they add uncertainty. All of the satellite's parts were therefore idealized. This meant making simplifications to the geometry, i.e. removing unnecessary holes, straightening out edges and filling in small gaps. Figures 4.8 and 4.9 show how the HSI platform part was idealized. The holes here are not removed but simplified as they are needed to define boundary conditions.

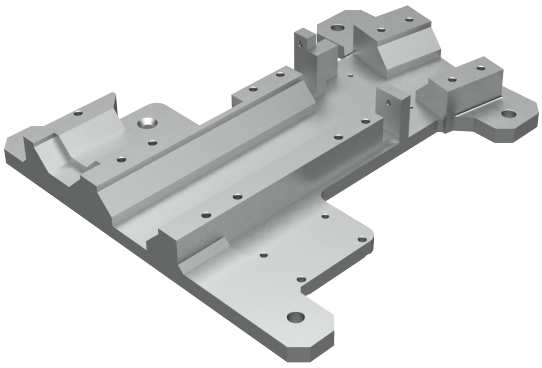

Figure 4.8: HSI Platform

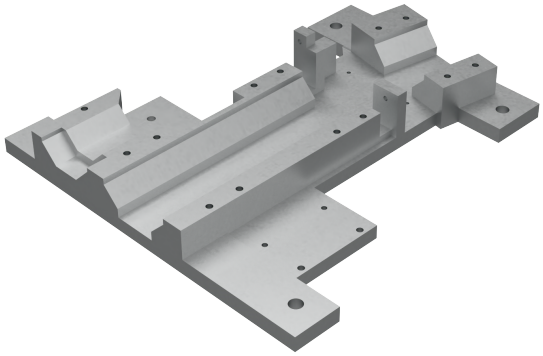

Figure 4.9: Idealized HSI Platform

Furthermore, some parts that were assembled from two or more connected components, have been merged into one single component. This was done by importing the bodies to the same part file and either applying a unite command, or by mating the mesh of the individual bodies together. The last one lets us apply different materials to the bodies and was therefore preferable in some cases. We did however choose to use the unite command on

some parts that consisted of the same materials. Both the HSI and RGB detector housings originally consisted of two bodies, but these were united together. Originally the 6U frame had multiple bodies, these were also united together. In order to make the frame as simple as possible, we also removed many of its screw holes, leaving only the necessary ones and reducing the frames density to counteract the increased volume. This change might make the frame stiffer.

The objective parts were originally solid bodies, and continuing without removing material inside would have made them heavier and stiffer than they really are. We could not find any technical drawings of the inside dimensions of these objectives, and therefore assumed some. Details were also removed on the surfaces, like the grooves and screws. In reality the objectives also consist of materials like glass for the optical parts, and steel for the screws. We decided including these details would have little impact on the results.

For further simplification, it was necessary to exclude the geometry of some components altogether. This applies to parts that were deemed less critical, and that would have little impact on the results of the simulations. Components that had to be removed for the simulation were replaced with point masses, so that their mass contribution to the satellite was still present. The point masses were located at the respective component's center of mass (CoM). The coordinates for each CoM were found using the measuring tool in NX. Tables 4.2 – 4.5 above give an overview of all the satellite's idealized components. In these tables, no materials are specified for components that became point masses, because these do not need material properties. The original model of HYPSO-1 is shown in figure 4.10 and the idealized model in figure 4.11.

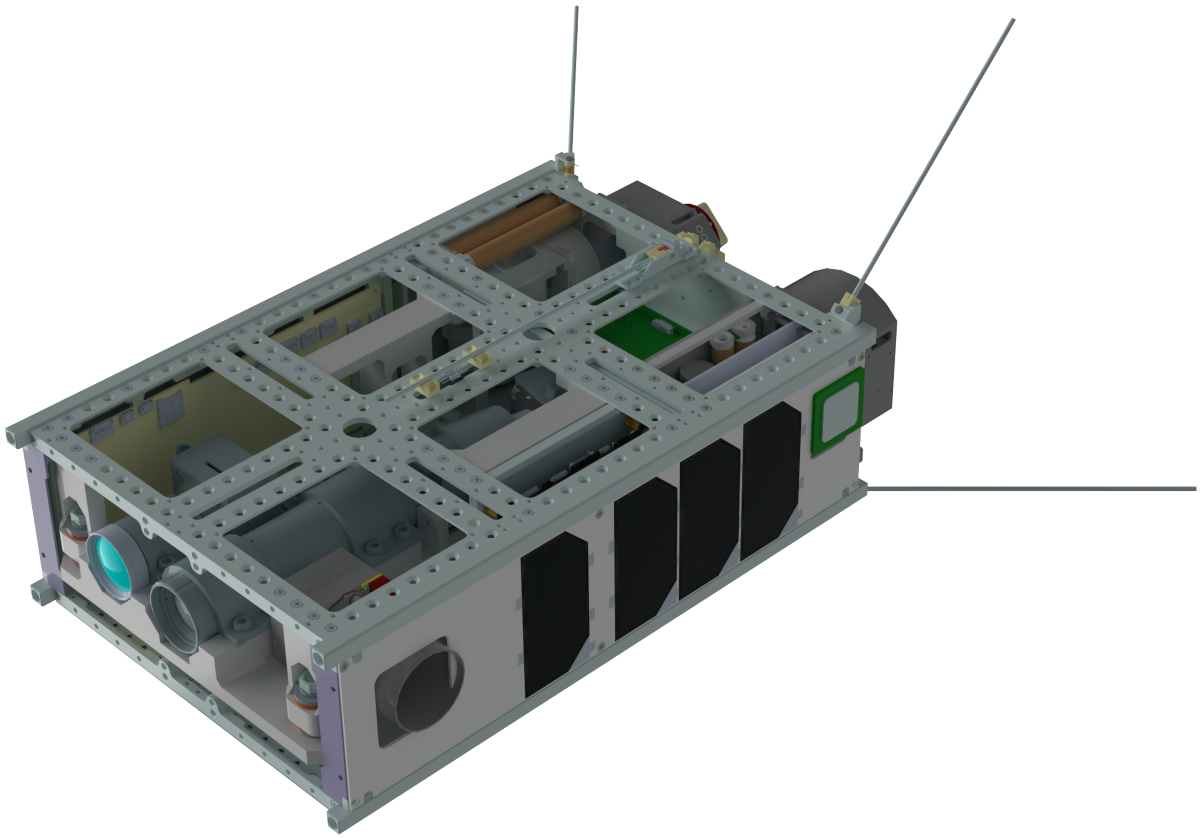

Figure 4.10: HYPSO-1

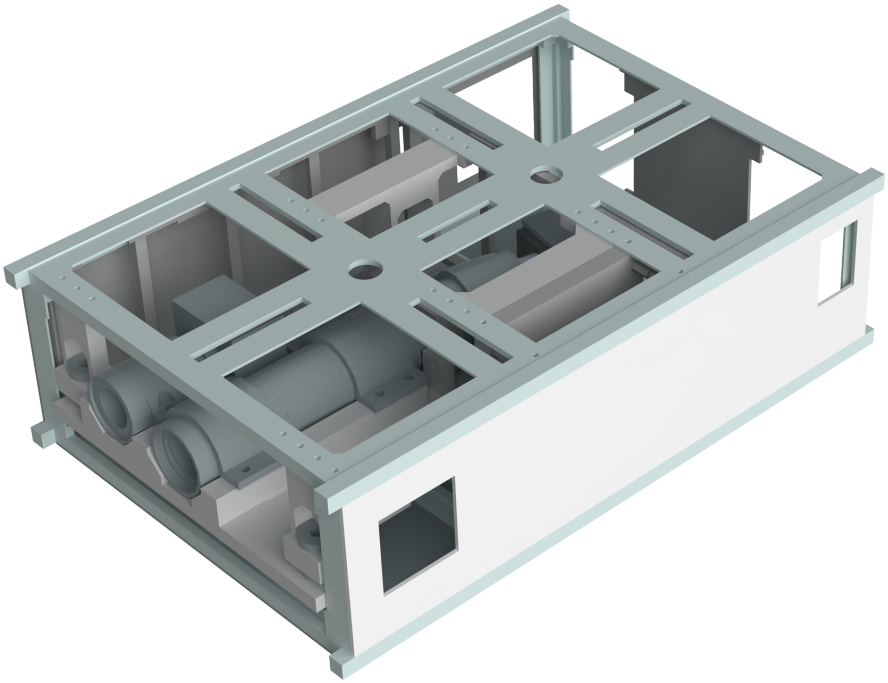

Figure 4.11: HYPSO-1 idealized

4.5 Mesh

The process of dividing the parts into a finite amount of smaller elements is called meshing. Choosing the right properties such as type, size, and shape are crucial in developing a good mesh that can achieve accurate results. For our NX FEM model there are many different mesh shapes to choose from. Since all the bodies of our model are considered solid, we chose to use 3D tetrahedral mesh.

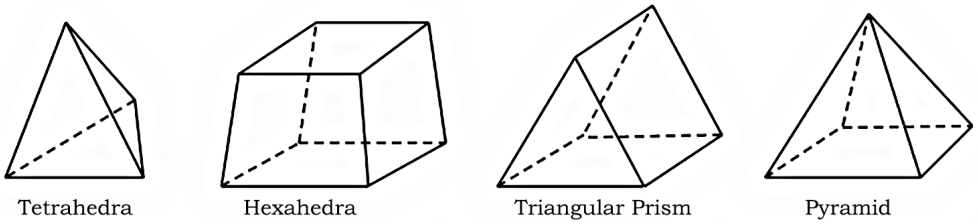

Figure 4.12: 3D mesh types. [36]

Element size seed was decided based on mesh convergence studies. Idealized parts that had important detailed geometry were given a greater curvature based size variation value. This means the elements are able to deviate even further from the base seed to capture these details. Some parts also had holes for bolt connections, here mesh controls were created which stayed constant throughout the convergence study. The values for these were decided based upon our experience, and they were the same for all bodies. For M2 holes the element size was set to 0.7 mm, for M6 holes it was set to 1.5 mm, and for all other holes it was set to 1.1 mm.

Mesh Convergence

Initial mesh element size seeds were based upon our experience, and the geometric body's size and complexity. Almost all preliminary generated mesh had minimum two elements through thickness (MTETT) enabled. This choice was based on an assumption that it would be the best alternative for all applications, which turned out to be wrong. A convergence study of four to five simulations with different seeds was done for each assembly. Figure 4.13 shows

the procedure we followed for the study. Tests were also conducted to study the effect MTETT had on the element count and results. The simulations were eigenvalue studies of the type free free checks. In NX that meant using SOL 103 (see section 5.1) with all six DoF free.

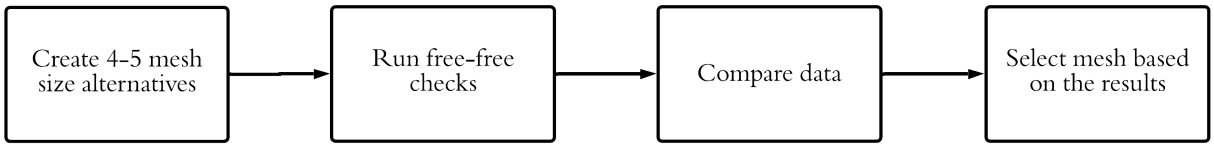

Figure 4.13: Our mesh convergence study procedure

As we study the results (see appendix C), we see that the frequencies between the largest and smallest mesh seeds do not vary too much. This could be because the mesh controls were enabled throughout the study, making the actual change in mesh size smaller than it would have been without them. When selecting the options to use, we must keep in mind that we want as few elements as possible while retaining the accuracy of the analysis. As we stated earlier in section 4.4, the more elements our simulation contains, the more equations the computer has to solve, which in turn makes the simulation more demanding.

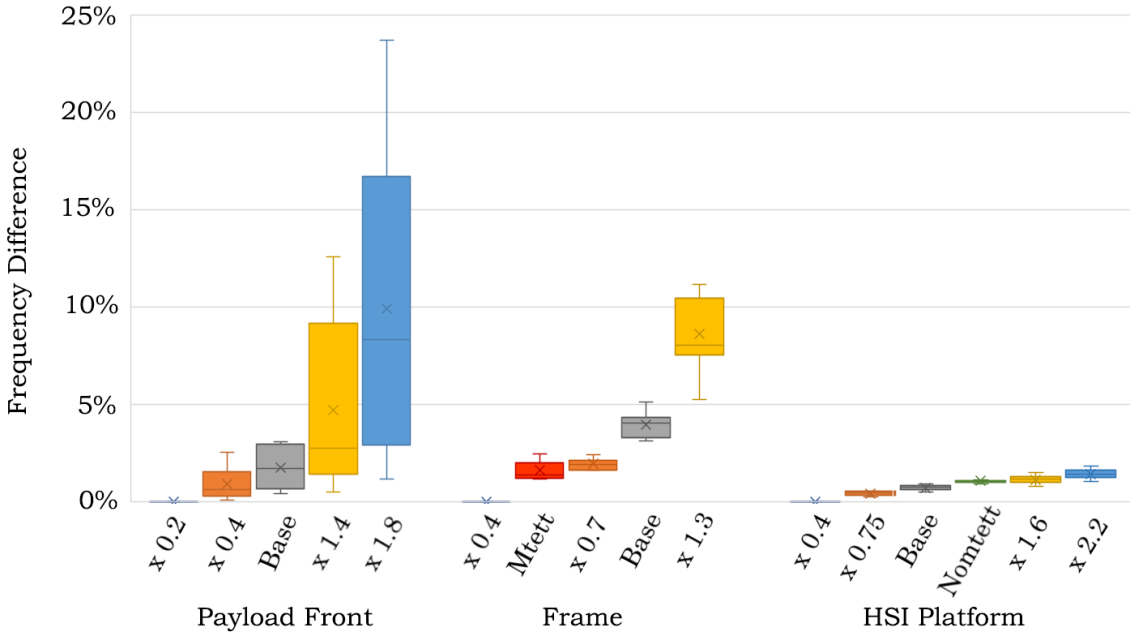

Figure 4.14: Mesh convergence results from a selection of parts. The y-axis shows the frequency difference for the first eight modes with regards to the finest option

Amongst all the studies, the front payload has the biggest variance in results. As shown in figure 4.14, the bigger mesh really deviates from the finer mesh. We chose sticking to the base seed as this gave us a nice balance between accuracy and complexity, reducing the number of elements by 29% from the finest mesh. Moving on, the base times 0.7 option was chosen for the frame, as this is where the results converge nicely. We can see the MTETT option is slightly better performing, but since it had more elements it was not considered.

For the cassette, platform, and picoBoB, the NOMTETT option was chosen. We found that the maximum deviation these options had from the finer mesh was within what we tolerated, and concluded that it would not have much impact on the results. Figure 4.14 shows the results of the platform, which look very similar to these other parts. The natural frequencies of the rear payload converge at around 1.4 times the base seed, with the biggest deviation being a 5% difference at mode 10. A test with MTETT turned off was run on the rear payload in hopes that we could push the element count down, but the differences were deemed too great even though it had the least amount of elements. A mesh seed size of base x 1.4 was therefore chosen for the rear payload. In total our model ended up with 290 654 tetrahedral elements.

4.6 Connections

The next step is to apply different connections between the parts. This is to restrict their number of degrees of freedom (DoF), and connect the parts together. Without these connections the parts would not interact at all and clip through each other. As we talked about earlier in section 4.4, some parts were united together which means they are already connected. There are however still a lot of parts left.

When applying some of these connections we had to choose between the rigid body elements (RBEs): RBE2 and RBE3. A rigid body is a collection of nodes, elements and surfaces that all depend on the motion of one single node. For RBE2 the relative position of the dependant nodes to the independent node remain constant throughout the simulation, making whatever this boundary condition is applied to infinitely stiff. RBE3 on the other

hand creates slave nodes that distributes the applied loads and mass to the connected nodes. This allows them to deform, which means it does not add additional stiffness to the model.

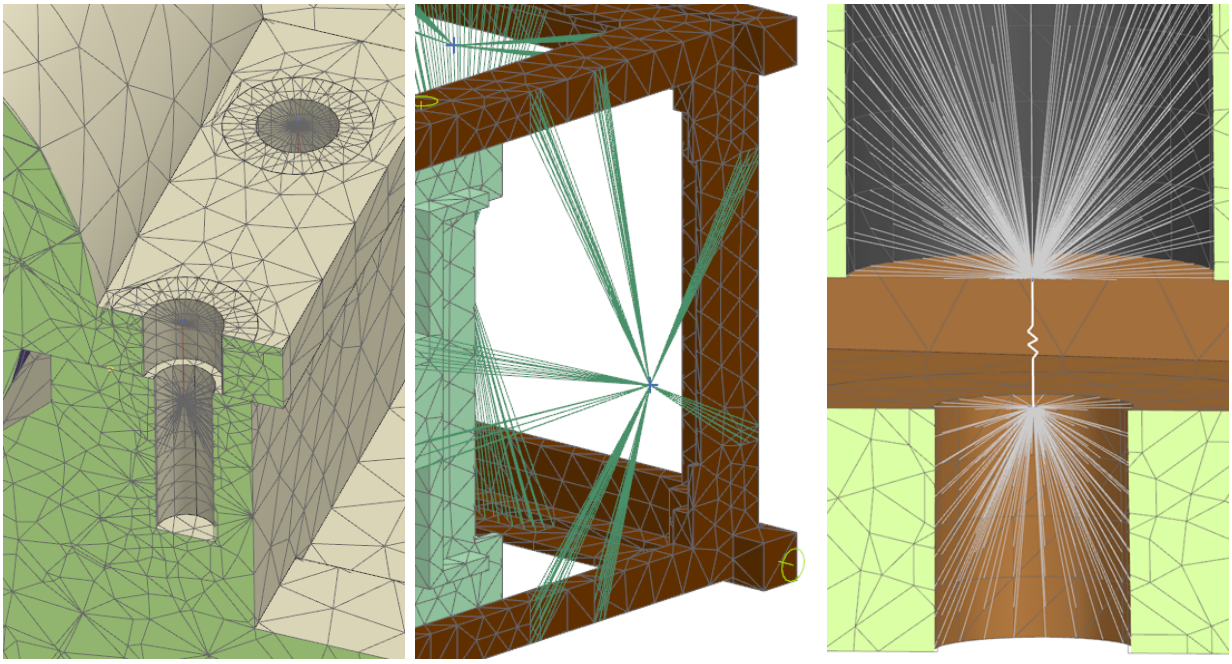

Figure 4.15: From left to right: section view of a bolt connection, point mass, section view of a damper connection

4.6.1 Surface to Surface

Surface to surface connections are as the name would imply, a connection between two surfaces. When applying these connections there were a lot of options to choose from. We have listed the alternatives we considered below.

Surface to Surface RBE2

We could apply surface to surface RBE2 connections, which would make whatever surfaces we selected infinitely stiff. Displacement and loads will therefore not be translated accurately. This is not a great option for us as it would make our simulation less realistic.

Surface to Surface Glue

This method translates displacement and loads between two meshed surfaces. The nodes of the surface mesh don't even have to be coincident, meaning they can be dissimilar. This was

a very good option for our simulations, but it was not used as it had to be applied at the sim-file level. Which would mean we would have to apply these connections for every new simulation, leading to a lot of unnecessary labor.

Mesh Mating

As we discussed in section 4.4, there also is the option to import bodies to the same part file, then mate the different bodies mesh together at the surfaces. This is a simple and effective solution that translates displacement and loads, and lets us apply materials to the individual bodies. This method was therefore primarily used for our simulations. The connection between the objectives and brackets, and RGB C-mount to detector housing are examples of this kind of connection.

4.6.2 Bolt Connections

For some of the screw connections in the model, tapped hole bolt connections were chosen. These connections were used where we thought more detail was important, e.g. the brackets to the payload, and crosslinks to the frame. Every bolt connection consist of a CBAR element that is connected to the model with RBE2s structured in a spiderweb-like fashion, as seen in figure 4.15 showing a bolt connection between a bracket and the platform. The CBAR element represents a cylinder, and is a one-dimensional simplified beam element that supports tension, compression, axial torsion and bending [37].

4.6.3 Point Masses

As stated in section 4.4, some of the components had to be removed and replaced with a point mass. Figure 4.15 shows a point mass connected to the rear frame. When creating these point masses, new points were added at the coordinates of each component's CoM. In order to give the points a weight, a zero-dimensional concentrated mass element (CONM2) was created at the location of the points. The CONM2 element was then connected to the model using RBE connections. In preliminary simulations, RBE2 elements were used for some of the stiffer point masses. This made the model stiffer than we wanted. Therefore the

RBE2 connections were replaced with RBE3, making this the only connection type we used for all the point masses. Table 1 in appendix A gives an overview of all the point masses in our simulation model.

4.6.4 Dampers

A CBUSH element is a generalized spring and damper connection. It is used to define a spring and damper structural element that may be frequency or nonlinear dependent. The CBUSH element is sufficient in defining stiffness along multiple degrees of freedom [38]. This is the connection we used to replicate the actual dampers of the model, and is seen in figure 4.15 connecting the platform and a rear crosslink together. Here the CBUSH element is connected to the parts via RBE2 elements.

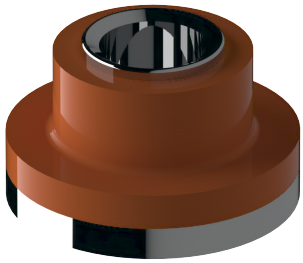

Figure 4.16: Rendering of the SMAC damper

The payload dampers are circular frequency isolators, and can be seen in figure 4.16. They consist of a base made of steel with an elastomer on top that dampens the vibrations. We know the dampers use SMACSIL as its elastomer material [39]. The only property we found on this material that is relevant for CBUSH elements is its axial stiffness of 95.9 N/mm [40]. This is not enough information to create a perfectly accurate representation of the dampers, which is why we mainly focused on simulations without CBUSH elements in this thesis. However, knowing the axial stiffness was enough information for us to be able to create a simulation. Since our main simulations are hard to compare to the physical tests, as the dampers are critical for the outcome, we decided to create one and compare it.

Chapter 5

Simulation

In this chapter we explain what choices were made when setting up the simulations. In the first section of the chapter we discuss the different solvers we could choose from in NX. The second section describes the three simulation models we made, and the differences between them. The third section gives an overview of the sensor locations in our models, and in the fourth and fifth sections we explain the different cases we simulated.

5.1 Solvers

NX Nastran comes with a large variety of solvers. These are all made for different load cases and provide different inputs and outputs, although some might overlap in terms of usability and function. When choosing which ones of these to use, we first needed to know what load case we wanted to simulate.

5.1.1 Dynamic Solvers

The first step of our study consisted of finding the natural frequencies and mode shapes of our model. For this we could neglect damping in the system [41], and therefore chose to use SOL 103. For the forced response tests, the linear and non-linear solvers in tables 5.1 and 5.2 were considered.

Table 5.1: Dynamic shock solvers

Forced Response Shock		
Solver	**Linear (Y/N)**	**Result Type**
SOL 103 RD	Y	Modal Transient Response
SOL 112	Y	Modal Transient Response
SOL 109	N	Direct Transient Response

Table 5.2: Dynamic random vibration solvers

Forced Response Random Vibration		
Solver	**Linear (Y/N)**	**Result Type**
SOL 103 RD	Y	Modal Frequency Response
SOL 111	Y	Modal Frequency Response
SOL 108	N	Direct Frequency Response

Linear solvers are not able to calculate material plasticity and body interaction [41], they are however faster than their non-linear alternative because their stiffness matrix remains static throughout the study. For nonlinear solvers, such as SOL 108/109, the stiffness matrix is dynamic, being influenced by nonlinear material and geometric stiffness. For the given tests, we are going to assume strictly linear behaviour is occurring. That means we can select one of the linear solvers, simplifying the problem and cutting down on processing time.

In SOL 111/112 you can define excitations and it will calculate the simulation models responses to these. The difference between SOL 103 and SOL 111/112 is that in SOL 103 we don't define any excitations. This means it doesn't actually calculate any responses, because no excitations are defined. What it does instead is calculate the modes of the simulation model and other matrices that can be used in a NX module called response dynamics (RD).

5.1.2 SOL 103 Response Dynamics

After attempting multiple simulations with the different solvers mentioned in tables 5.1 and 5.2, we found that SOL 103 RD best served our needs. Together with RD, it determines the static or dynamic responses of a structural model subjected to various loading conditions using modal approaches. With SOL 103 RD, we can define SRS and PSD functions, that can be used for analysis. Therefore, this option was primarily used for our simulations.

Peak Response Calculation Method

In regards to shock testing, SOL 103 RD is a useful tool for calculating the peak response acceleration of a single node. Using the SRS function containing the test requirements, a translational nodal excitation can be applied to a response spectrum event. For the shock simulations in SOL 103 RD, NX comes with the following five options for how the software will compute the peak response value:

- Absolute value
- Square Root of the Sum of the Squares
- Naval Research Lab method
- Complete Quadratic Combination
- Nuclear Regulatory Commission

We chose the square root of the sum of the squares (SRSS)-method for our shock simulations. With this method the software assumes that the modal responses are uncorrelated and the various peak responses will occur at different times. Because the physical shock tests were performed by applying one shock pulse at a time, we concluded that SRSS would give the most accurate results for comparison with these tests. We also considered the absolute value method as an option for getting conservative results, in which case the software assumes a worst case scenario where all modal peak responses occur simultaneously with all modes in phase [42].

5.2 Set-Up

Since the plan is to launch the HYPSO spacecraft with a SpaceX Falcon 9 rocket, we will define our shock and vibration simulations based on requirements made by SpaceX and NanoAvionics. Prior to this thesis, the HYPSO-team performed physical shock, resonance and vibration tests at the Norwegian Defence Research Establishment (FFI) premises. These experiments were done twice: once with the engineering model (EM), and once with the QM. Both these models consisted of a functioning payload, and mass models for the remaining components of the satellite. For these tests the frame was fixed in all six DoF to a test table as shown in figure 5.1. For every experiment, three tests were conducted, once per BRF-axis [2]. Since the QM should, according to NanoAvionics, be practically identical to the flight model (FM), we will use this model for comparisons.

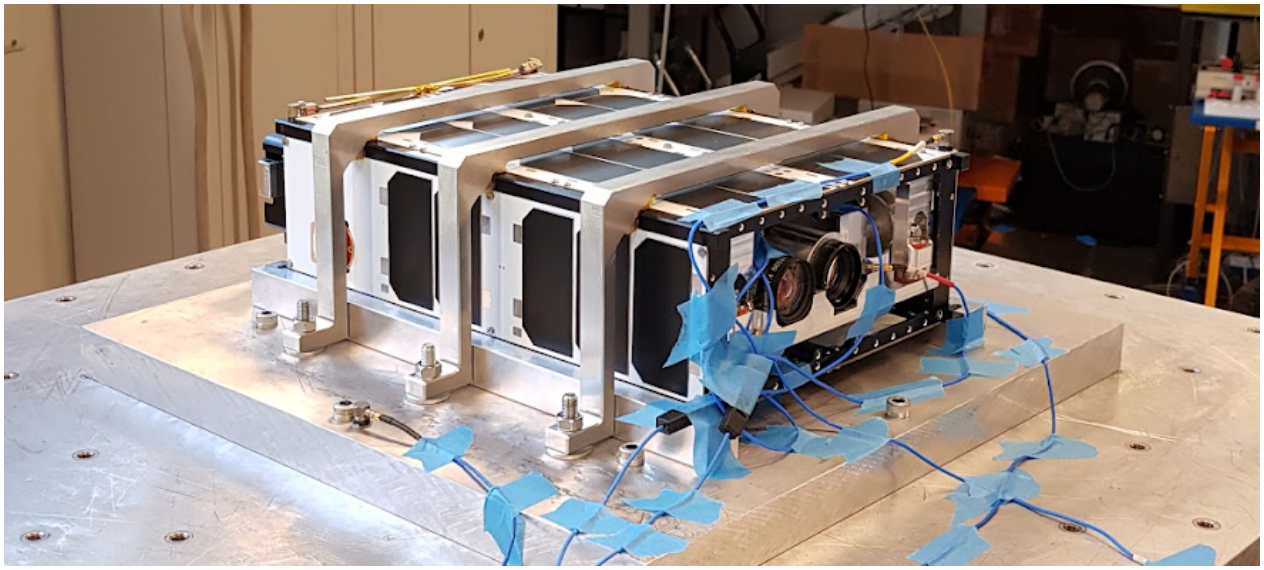

Figure 5.1: Mechanical test setup

Initially we made two different simulation configurations, which are described below in section 5.2.1 and 5.2.2. These did not contain the dampers connecting the platform to the crosslinks (see 4.6.4). Our models compared to the real satellite should therefore be stiffer and experience greater acceleration peaks. The simulation models do however have a Q-factor of 10 applied, which is the hysterical (mechanical) damping in the system equal to

5% [43], but this barely has any effect on the results. Due to the inaccuracy caused by the absence of dampers, we also made a third simulation configuration that included these, which is further explained in section 5.2.3.

5.2.1 Fixed Model

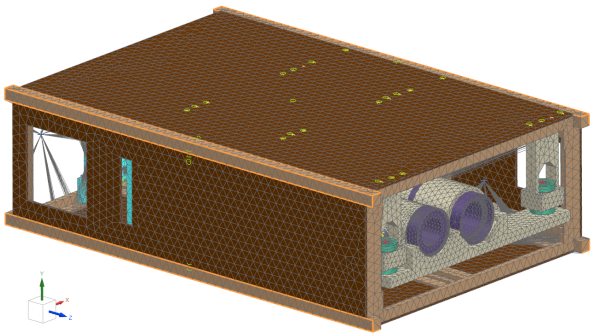

Figure 5.2: Simulation model with fixed constraints

In the first simulation model, a fixed constraint was applied on the surfaces of the frame that were rigidly fastened to the test bench. Which means that the table itself and the mounting brackets do not have to be included. This model is shown in figure 5.2 where the fixed faces are highlighted. The advantage of this is that the mass of the table and brackets does not affect the modal frequencies obtained from the resonance study. It is important to keep in mind that the fixed constraints are not perfectly accurate representations of the fastening, because they make the frame faces completely unable to move in any of its six DoF.

5.2.2 Test Bench Model

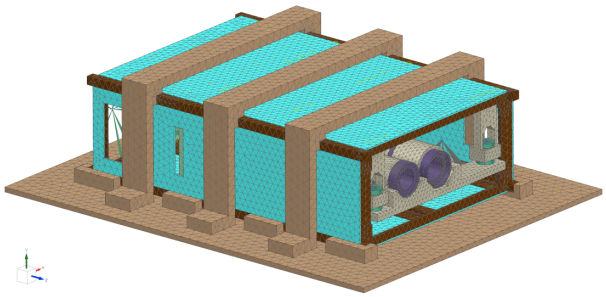

Figure 5.3: Simulation model with test bench set-up

Since the mounting plate and brackets will in reality also experience slight deformations together with the satellite, we decided to make a second simulation model, which includes the test plate and brackets. This means that the frame is not completely fixed in all DoF, as opposed to the first configuration. Compared with the fixed configuration, it is a more precise replication of the physical test scenarios, and should give results that are closer to the physical results. However, the mass and stiffness of the virtual test table and brackets will influence the modal frequencies.

5.2.3 Damper Model

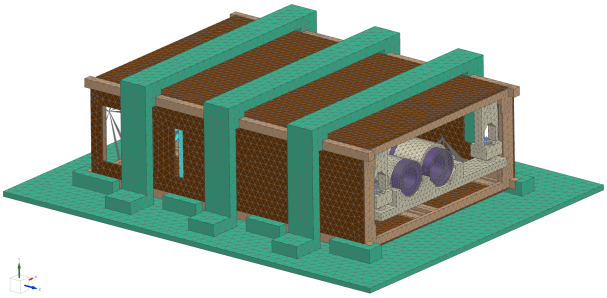

Figure 5.4: Simulation model with test-bench set-up and damper elements

We know the two models above will yield much stiffer results than what is realistic for the satellite. This is, as mentioned, partly because they lack elements that simulate the damping effect of the dampers in the system. Therefore, we created a third model where CBUSH elements replaced the stiff connection the crosslinks had to the platform. We defined the axial stiffness to 95.9 N/mm in all three BRF axis, which is the axial stiffness of SMACSIL — the elastomer material used in the dampers of HYPSO-1. As already mentioned, more information on the damper is needed for the damper model to be sufficiently comparable with the physical model. Therefore, the results from simulations using the damper model cannot be expected to match the physical test results, but they can be used for illustrating the effect of damping when compared with results from the two undamped configurations.

5.3 Sensors

In order to obtain comparable results from our analysis we created sensors at the same locations as they were placed in the physical tests. In the simulations these are not actual sensors with mass and inertia, rather we are telling NX to output the acceleration data at the selected nodes. There are in total six sensor nodes and their placements are shown in figure 5.5.

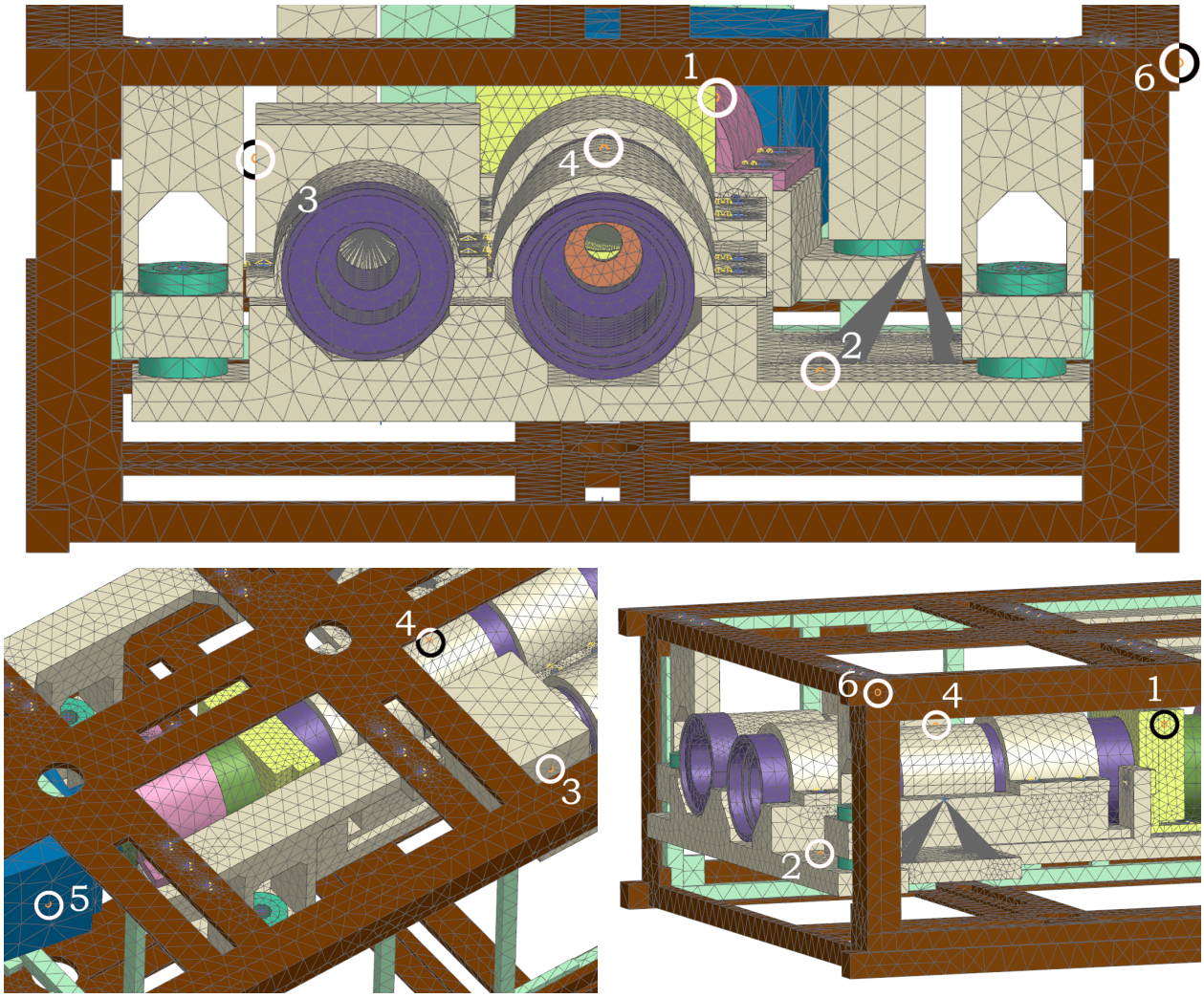

Figure 5.5: Placement of sensors in FEM. (1 – cassette, 2 – platform, 3 – RGB detector, 4 – slit tube, 5 – HSI detector, 6 – Frame)

5.4 Resonance

To validate the FEM, we had to compare the natural frequencies of our model to the ones found during testing. While the physical sine sweeps were run three times per axis, once at the start, then once after every forced response test [2], [44], we will only compare our results to the first sweeps. This validation is important because it tells us how accurate our shock and vibration studies can be. Ideally we want our natural frequencies to be as close to the experimental response frequencies. We know however that this won't be the case, because as we said above, our model does not simulate the payload dampers.

5.5 Testing Profiles

An overview of the different load cases we need to test for is given in table 5.3, where some numbers are based on the MPE during launch and some on "acceptance", which is the tests the FM has to go through. The MPE derive from NanoAvionics' ground testing, flight data, and vibroacoustic models [22]. All three BRF axes of the satellite will be tested in our simulations.

Table 5.3: Qualification tests and procedures overview from NanoAvionics [22]

Test	**Qualification Approach**
Shock	6 dB above MPE, 3 times in each of 3 orthogonal axes
Random vibration	6 dB above acceptance for 2 minutes in each of 3 axes

5.5.1 Random Vibration

The simulation for random vibrations will use values based on the random vibration maximum predicted environment (MPE). Here all flight events influences the MPE, and not only the last three as for shock. Again we will look at the Falcon 9 requirements.

Table 5.4: Nanosatellite random vibration MPE produced by the Falcon 9 [22]

Frequency [Hz]	**Random Vibration [g^2/Hz]**
20	0.0044
100	0.0044
300	0.0126
600	0.0126
740	0.036
850	0.035
2000	0.0064
G (RMS)	5.48

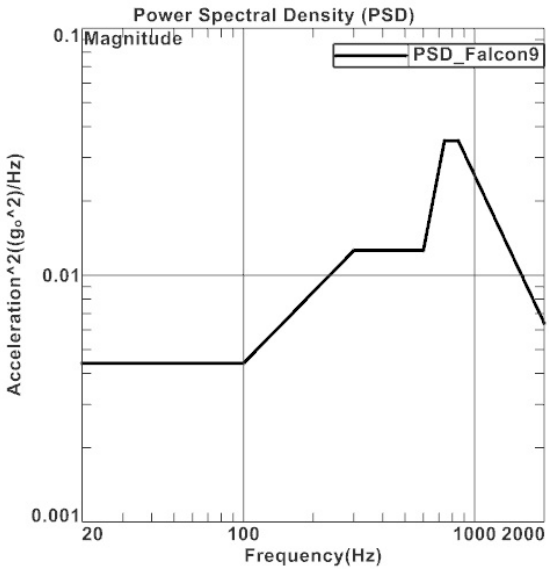

5.5.2 Shock

We will run two shock simulations. One will use the same values as the physical shock test that was conducted by the HYPSO team, shown in table 5.5.

Table 5.5: Shock test values used by the HYPSO team [2]

Frequency [Hz]	**SRS [g]**
100	30
600	300
2000	300

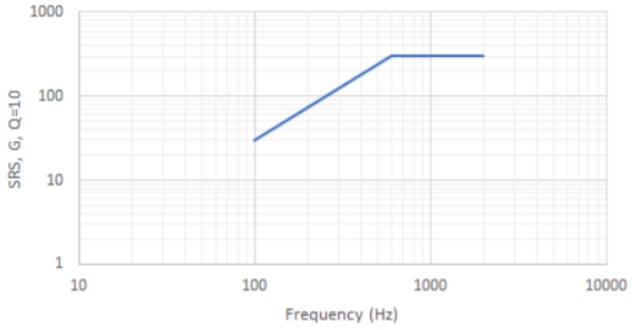

The other shock simulation will use the values given by NanoAvionics which are shown in table 5.6. These values are based on the MPE at the satellite's position in the rocket during the fairing deployment and co-nanosatellite separation events [22].

Table 5.6: Nanosatellite mechanical shock induced by the Falcon 9 launch vehicle and co-nanosatellite(s) [22]

Frequency [Hz]	**SRS [g]**
100	30
1000	1000
10000	1000

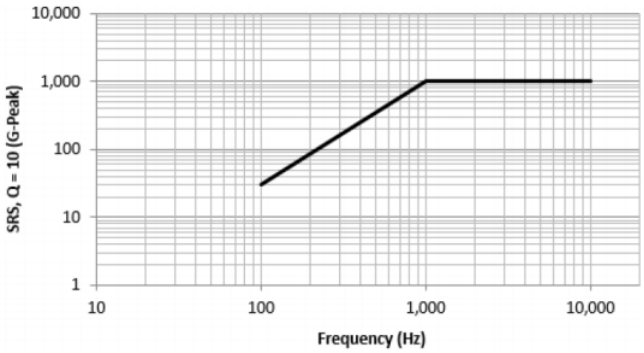

Chapter 6

Results and Discussion

This chapter presents the results from our simulations. Comparisons between simulation results and test results are made in order to evaluate the accuracy of our simulations. Where there is a deviation between simulation results and test results, we reflect on the possible reasons why.

6.1 Modal Check

After running the simulations, the resonance frequencies of the model are given, together with information about the respective mass participation. This means it calculates the modes irrespective of the BRF axes. We therefore have to look at the mass participation of the frequencies in each axis so we can compare them to the ones found from the physical tests, which were found running sine sweeps in each axis. If a frequency had a mass participation of more than 0.1% in an axis, it was counted as a natural frequency of said axis. In table 6.1 we can compare the resonance frequencies of our simulation models to the real frequencies found from physical testing. The full list of resonance frequencies can be found in appendix D.

Table 6.1: Comparison of the obtained resonance frequencies

Axis	**Physical Test (QM)**	**Fixed Model**	**Test Bench Model**	**Damper Model**
X [Hz]	76, 150, 223, 291	271, 365, 938	223, 231, 438, 481	71, 375, 397
Y [Hz]	125, 225, 330, 405, 535*	321, 365, 407, 443, 521, 527	307, 353, 384, 438, 505, 515	75, 375, 397, 422, 480, 512
Z [Hz]	82, 148	234, 407, 521, 527	223, 231, 384, 481, 505, 515	70, 137, 375

* Y-axis values for QM read from plot

We see that our fixed and test bench models have much higher first natural frequencies than the physical model. This is likely because the physical model has dampers installed. We believe there are mainly two reasons for the lower natural frequencies of the test bench model compared to the fixed: the added mass of the test bench and brackets, and removal of the frame fixtures (meaning the frame is not infinitely stiff anymore). Our damper model is the only model that produces results comparable to the first frequency of the real test. It does however not look like it keeps up well for the second mode in the x and y axes. The results from the damper model should be taken with a grain of salt though (see section 4.6.4).

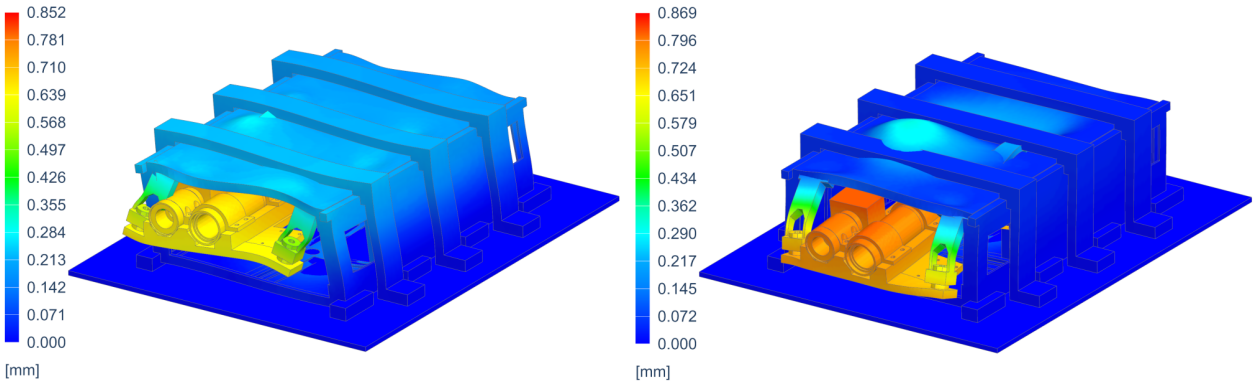

Mode 1 (223 Hz)

Mode 2 (231 Hz)

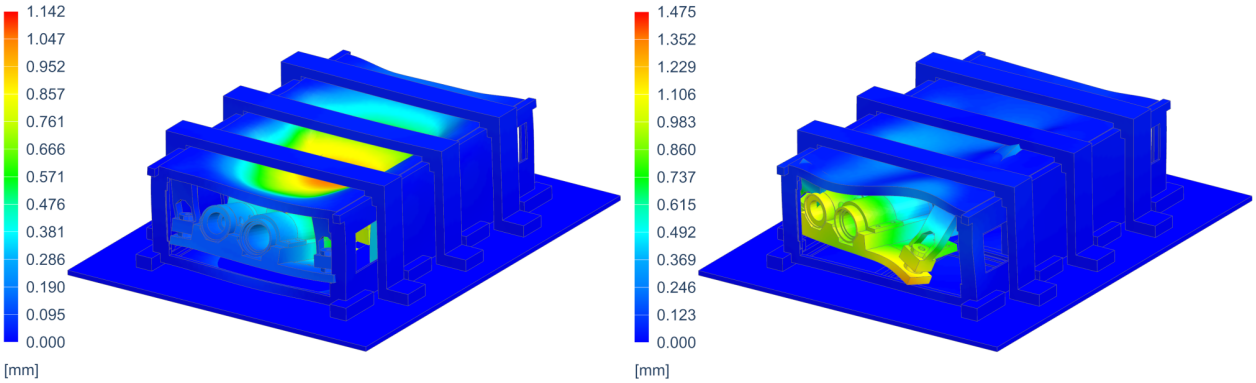

Mode 3 (307 Hz)

Mode 4 (353 Hz)

Figure 6.1: The first four eigenfrequencies and mode shapes for our test bench model with exaggerated deformations

As seen in figure 6.1, the first mode of the test bench model occurs at 223 Hz with the highest participation factor in the x-axis. The second mode has the highest participation in the z-axis and occurs at 231 Hz. Here we can observe that the payload cameras experience quite some deflection. Mode three (307 Hz) and four (353 Hz) have the highest participation in the y-axis. What all four modes have in common is that the maximum deflections occur at the HSI detector. This could indicate that the HSI detector is the most exposed part of the satellite.

6.2 Random Vibration

Studying the structural responses caused by subjecting our model to the random vibration event described in section 5.5.1, we can see that our results have some differences from the experimental data (see appendix E for all the random vibration plots). As we mentioned earlier, this comes as no surprise as we did not have enough data on the dampers. We have identified the HSI detector as the most vulnerable component of the satellite. We see this both from our simulations, and physical testing. This is therefore primarily the component we will look at. Table 6.2 shows the peak responses of the HSI detector in our simulations compared to the physical tests.

Table 6.2: Comparison of the peak response values of the HSI detector for the random vibration event

Axis	**Frequency [Hz] - Peak Response [g^2/Hz]**			
	Physical Test (QM)	**Fixed Model**	**Test Bench Model**	**Damper Model**
X	71 - 0.076	271 - 6.380	223 - 8.002	71 - 1.899
	130 - 0.184	360 - 0.170	481 - 1.240	167 - 0.001
Y	120 - 0.308	321 - 16.310	300 - 16.459	75 - 1.829
	244 - 0.105	435 - 0.270	515 - 4.510	140 - 0.003
	332 - 0.261	527 - 3.980		375 - 0.015
Z	73 - 0.053	234 - 2.650	231 - 2.641	70 - 1.718
	128 - 0.069	525 - 0.080	505 - 0.114	140 - 0.002

We see that our simulations get much higher peaks compared to the physical tests, where the test bench model experiences the highest acceleration loads. Its biggest deviance from the physical results happens for the first peak in the x-direction where it experiences acceleration 105 times greater than the QM, while the y and z directions are 53 and 50 times greater, respectively. This can also be seen in figure 6.2. The damper model results

have the lowest peak values among the simulations, but they are still not very realistic. With accelerations 25, 6, and 32 times greater than physical results in the x, y, and z direction.

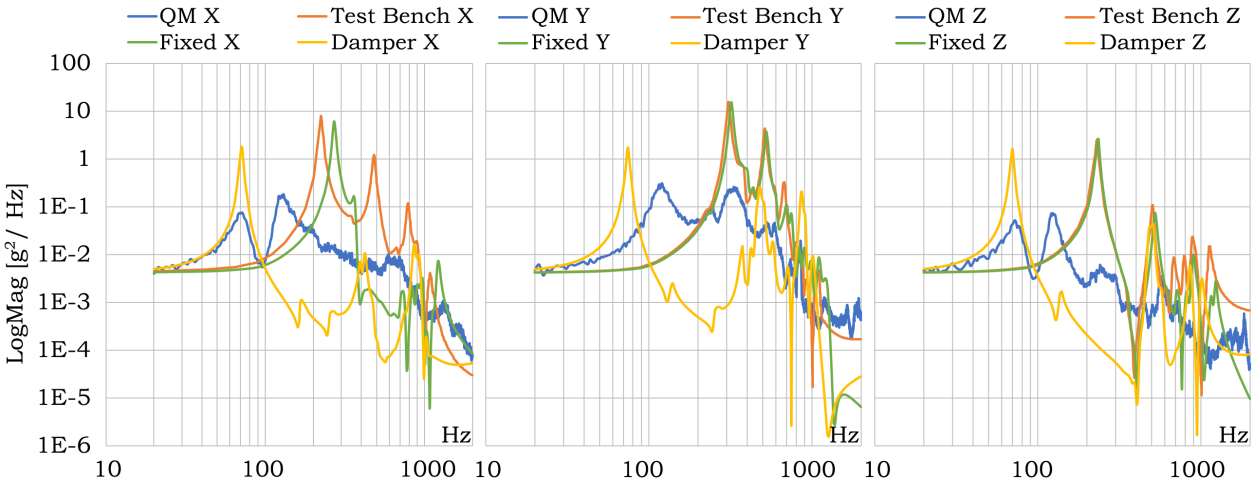

Figure 6.2: Random vibration response comparisons of the HSI Detector in all three axes

Although the undamped simulation results currently are too stiff to properly compare, there are still some similarities. The HSI detector remains exposed to higher acceleration loads after the first mode, than the other components in the y-direction (this is better seen in figure 6.3 below). We also see that the physical responses generally start with two powerful peaks, followed by diminishing unsynchronised behaviour among the parts. We see this same pattern in our simulations (see figures 6.3, 6.4, and 6.5). We know from section 6.1 that they have a few somewhat shared natural frequencies where we see higher and narrower acceleration peaks for the undamped models, which is expected differences between a damped and undamped system [45].

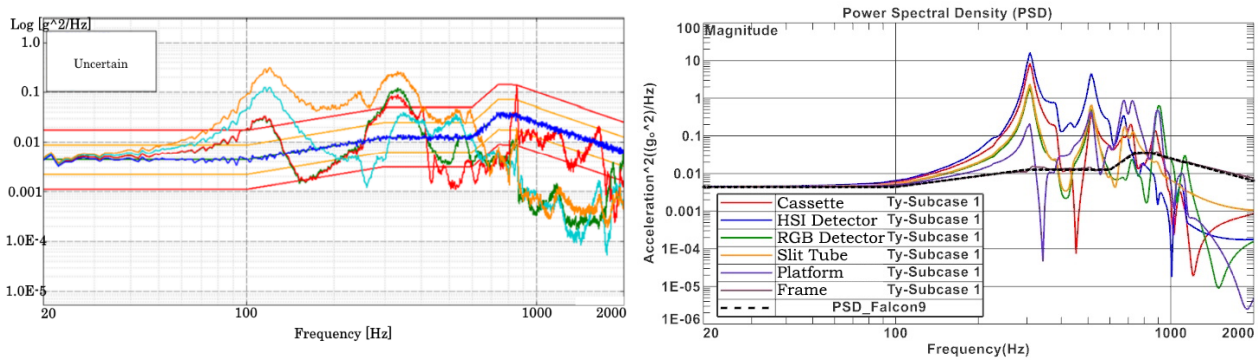

Figure 6.3: Comparison of QM (left) and test bench model (right) random vibration responses in y-direction

Discussion

Higher acceleration peaks for our simulations can be the product of many factors. Idealization, mesh sizes, connections, and the absence of dampers are all factors we need to consider. Changes to geometry, like removing holes in the frame and connecting components with mesh mating that should in reality be screwed together, should make our models stiffer. Our simulation models are also towards the lighter side of what the physical satellite is estimated to weigh, which also does not help. We saw that the model became stiffer with bigger element sizes. Although we did run a study and chose sizes that gave us relatively little deviation from the finest result, we do not know what effect combining all the parts together gives. We also do not know if our finest options gave an accurate result in the first place, because we have no real world tests to compare with on an individual component level.

For the damped model the first modes approach a more realistic frequency value, which we could also see in section 6.1. The peak accelerations are also reduced. It does however miss a lot of peaks in the mid-range, and the response accelerations are still noticeably higher, confirming that the damping model still needs some work.

Test Bench Model

For all our random vibration simulation result plots see appendix E. The following figures display the QM responses and our test bench model responses in x and z direction.

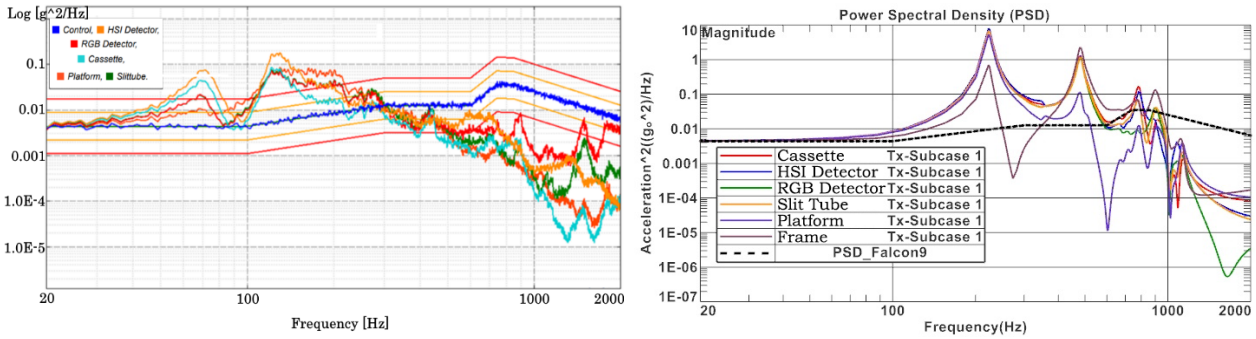

Figure 6.4: Comparison of QM (left) and test bench model (right) random vibration responses in x-direction

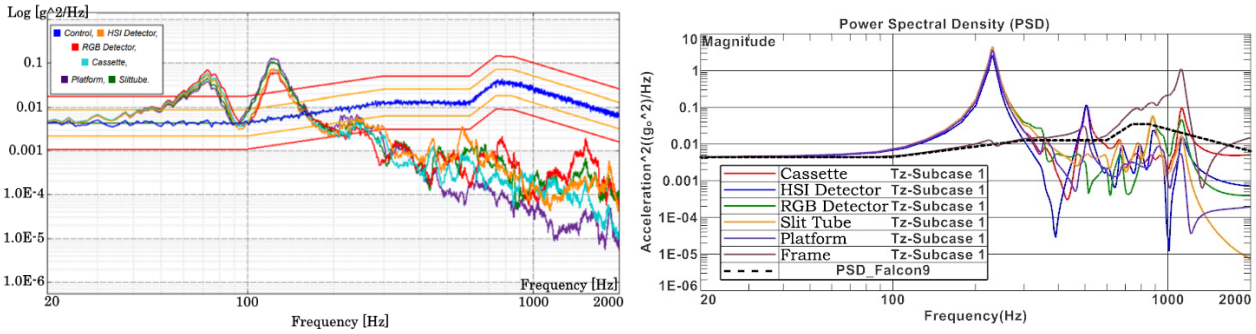

Figure 6.5: Comparison of QM (left) and test bench model (right) random vibration responses in z-direction

6.3 Shock

After simulating the shock event, NX only provided results from the sensor node that experienced the highest peak acceleration. In order to find the response at each individual sensor, it was therefore necessary to perform multiple simulations with one sensor selected at the time. Due to time constraints, we only performed simulations for the HSI detector sensor, as this was considered the most critical component. The results are tabulated in table 6.3 and 6.4. The tables show the simulated peak response accelerations next to the peak responses that were measured during physical tests. Appendix F contains graphs that show the shock response spectra measured by all the sensors that were mounted during physical testing.

Table 6.3: Comparison between the physical test results and simulation results with fixed constraints

	Physical Test (QM)	**Fixed Model**	**Difference**
Peak Response [g], X	150	134.5	15.5 (-10%)
Peak Response [g], Y	190	339.9	149.9 (+79%)
Peak Response [g], Z	80	80.77	0.77 (+1%)

Table 6.4: Comparison between the physical test results and simulation result with the test bench

	Physical Test (QM)	**Test Bench Model**	**Difference**
Peak Response [g], X	150	166.8	16.8 (+11%)
Peak Response [g], Y	190	347.4	157.4 (+83%)
Peak Response [g], Z	80	86.84	6.84 (+9%)

Discussion

As displayed in tables 6.3 and 6.4, the results from our simulations are not completely consistent with the physical test results, as the response acceleration in the y-direction was increased by around 80% compared to the testing. However, the simulated shock responses in the x- and z-direction appear to be a lot more realistic, as the change is within approximately 10% from the results measured during the tests. Some difference between simulation results and test result were expected, because our simulations did not include dampers. The fact that shock simulations in the y-direction give the largest offsets from physical test results, strengthens the theory that dampers are necessary for the simulations to be realistic, because the dampers on HYPSO-1 are mounted vertically and therefore will give the highest damping effect along the y-axis.

Damper Model

Given the suspicion that dampers were necessary for results to be realistic, we also performed shock simulations on the model that includes dampers. However, as stated in section 4.6.4, this has some uncertainty related to it. The results of the simulations with dampers are tabulated in table 6.5 along with results from physical testing.

Table 6.5: Physical test results, simulation results with dampers and the difference between them

	Physical Test (QM)	**Damper Model**	**Difference**
Peak Response [g], X	150	20.1	129.9 (-87%)
Peak Response [g], Y	190	102.1	87.9 (-46%)
Peak Response [g], Z	80	35.8	44.2 (-55%)

Judging from these results, the damping effect appears to be highly exaggerated in our simulations, as shock responses are up to 87% lower than what was measured during physical tests. An important concern is that the largest offsets from the test results are the responses in x-direction and z-direction, which suggests that the dampers give the simulated model unrealistic amounts of shock absorbing in these directions. It turns out that the undamped models have delivered more realistic results than the damped model for the x- and z-axis.

6.4 Shock Qualification

The physical tests by HYPSO were not performed to the full Falcon 9 qualification standards stated by SpaceX and NanoAvionics. The FFI facilities were not able to reach the required g-level during the shock test, which is 1000 g. The shaker table could only output 300 g. NanoAvionics have stated that shocks with an amplitude of 900 g are possible at actual launch [2]. We have therefore decided to run simulations with the qualification requirements.

In a simulation these test values are achievable, and we were successfully able to run simulations with the Falcon 9 requirements. Table 6.6 tabulates the peak acceleration response in each axis, in each different model. The node under evaluation is the sensor node located on the HSI detector. There have not been performed physical tests using these requirements, so we have nothing to compare them to in order to validate them.

Table 6.6: Results from the Falcon 9 qualification tests

	Fixed Model	**Test Bench Model**	**Damper Model**
Peak response [g], X	203.6	232.7	56.0
Peak response [g], Y	490.2	507.8	213.4
Peak response [g], Z	140.1	133.6	68.8

The purpose of these particular tests was to determine whether the HSI Detector could withstand the Falcon 9 shock requirements. The results clearly show that the requirements are fulfilled, due to the fact that no peak responses surpassed the maximum value of 1000 g.

Chapter 7

Conclusions

Utilizing simulations to test current and future satellites, could potentially save the NTNU SmallSat team valuable time. The current simulation model is not perfectly accurate, and when compared with the physical tests, the results show that our simulated models experience higher response accelerations to shock and vibrations. However, it will be helpful for the SmallSat team in the future, as all the knowledge gathered in this thesis will be available, and our models can be improved upon.

For the random vibration forced responses, many of the acceleration peaks were higher than what was found during actual testing, with one peak 105 times greater than the physical result. There could be many reasons for this, with the most important being the exclusion of dampers. The idealizations and simplifications of parts and connections might also be contributing factors. The model that included dampers provided results that were significantly closer to the test results with peak accelerations reduced. They are however still greater than the physical test results. This suggests, as expected, that dampers are necessary for simulations to be comparable with physical test, although the damped model still has more potential in terms of accuracy.

For the shock simulations on the undamped models, the results were reasonable in the x and z axes, with the acceleration peak differences not surpassing 11% of the physical tests. However, the difference in results for the y-direction was much greater. After including dampers, the response accelerations were dramatically reduced, and ended up considerably lower than in physical testing, confirming that some improvements can be made to the dampers in the simulations:

Simulations are by no means a replacement for physical tests, but with careful adjustments and validation they could produce more reliable results. Having simulation models readily available will allow the team to discover how changes to the design impact the resonance frequencies and responses to shock, without having to run multiple physical tests for each change. This will help the design phase of future satellites, as it is much cheaper to run simulations on a virtual model than tests on a physical one.

Chapter 8

Future Work

Although we have managed to create a model that reacts similarly to the real satellite, there is still some work left to do. We believe the following points should be prioritized with regards to future shock and vibration testing and simulation.

- Run new physical tests of the satellite with no dampers. Results from these tests will allow for easier validation of parameters for the simplest case of the simulation.
- Acquire sufficient damper information to properly define them in simulations, and thereby improve the accuracy of a damped simulation model. (Will make simulations more useful to the project).
- Find a way to run shock simulations providing valuable results from more than one sensor node at a time.
- Run shock simulations using the absolute value method for peak response calculation (described in section 5.1.2). This will give worst case scenario results, and should be done when simulations can be made with realistic dampers.
- Run shock simulations on the rest of the sensor nodes. The peak response acceleration on the other components can be compared to the physical test results, providing further validation for the FEM model.

References

[1] *Mission: Hyper Spectral Camera - NTNU*. [Online]. Available: https://www.ntnu.edu/ie/smallsat/mission-hyper-spectral-camera (visited on 03/11/2021).

[2] M. Hjertenæs, E. F. Prentice, and T. H. Kaasa, "HYPSO-TRP-VIB-003: Shock, Resonance, and Vibration of CLAW-1 QM," NTNU, Tech. Rep., Sep. 2020.

[3] P. Kahn, T. Imken, J. Elliot, B. Sherwood, A. Frick, D. Sheldon, and J. Lunine, "Environmental design implications for two deep space SmallSats," in *Acta Astronautica*, vol. 139, Elsevier, 2017, pp. 390–395.

[4] A. C. Tribble, *The Space Environment: Implications for Spacecraft Design*. Princeton University Press, 2003.

[5] *Micrometeoroids and Orbital Debris (MMOD) | NASA*. [Online]. Available: https://www.nasa.gov/centers/wstf/site_tour/remote_hypervelocity_test_laboratory/micrometeoroid_and_orbital_debris.html (visited on 04/27/2021).

[6] K. Lemmer, "Propulsion for CubeSats," in *Acta Astronautica*, vol. 134, Elsevier, 2017, pp. 231–243.

[7] E. Mabrouk, *What are SmallSats and CubeSats? | NASA*. [Online]. Available: https://www.nasa.gov/content/what-are-smallsats-and-cubesats (visited on 03/11/2021).

[8] M. N. Sweeting, *Modern Small Satellites-Changing the Economics of Space*, 2018. (visited on 04/21/2021).

[9] T. Wekerle, J. B. Pessoa Filho, L. E. V. L. d. Costa, and L. G. Trabasso, "Status and Trends of Smallsats and Their Launch Vehicles — An Up-to-date Review," *Journal of Aerospace Technology and Management*, vol. 9, no. 3, pp. 269–286, Sep. 2017, Publisher:

Departamento de Ciência e Tecnologia Aeroespacial, ISSN: 2175-9146. DOI: 10.5028/jatm.v9i3.853.

[10] H. Shaftel, "Just 5 questions: SmallSat technology – Climate Change: Vital Signs of the Planet," Dec. 2013. [Online]. Available: https://climate.nasa.gov/news/936/just-5-questions-smallsat-technology/ (visited on 03/30/2021).

[11] B. Virgili and H. Krag, "Small Satellites and the Future Space Debris Environment," Jul. 2015.

[12] *Building and testing spacecraft*. [Online]. Available: http://www.esa.int/Science_Exploration/Space_Science/Building_and_testing_spacecraft (visited on 05/14/2021).

[13] G. Lu and B. Fei, "Medical hyperspectral imaging: A review," *Journal of Biomedical Optics*, vol. 19, no. 1, p. 010 901, Jan. 2014, Publisher: International Society for Optics and Photonics, ISSN: 1083-3668, 1560-2281. DOI: 10.1117/1.JBO.19.1.010901.

[14] *PSI Technics - Hyperspectral Imaging*. [Online]. Available: https://www.psi-technics.com/EN/Services-Products/Industrial-Image-Processing/Hyperspectral-Imaging.php (visited on 03/15/2021).

[15] C. Chang, *Hyperspectral Imaging: Techniques for Spectral Detection and Classification*. Kluwer Academic/Plenum, 2003.

[16] *Landsat sensors: Pushbroom vs whiskbroom*, Oct. 2017. [Online]. Available: https://svs.gsfc.nasa.gov/12754 (visited on 04/21/2021).

[17] *Landsat 9 Instruments: Pushing into the future*. [Online]. Available: https://landsat.gsfc.nasa.gov/landsat-9/instruments (visited on 04/21/2021).

[18] D. Langer, *Image registration and georeferencing with snapshot camera for the HYPSO mission*, Jun. 2019.

[19] P. Rivera, "Dynamic Response Validation of CubeSats through Testing and Finite Element Analysis," California Polytechnic State University, San Luis Obispo, California, Tech. Rep., Jun. 2019. DOI: 10.15368/theses.2019.40.

[20] S. H. Crandall and W. D. Mark, *Random Vibration in Mechanical Systems*. Academic Press, 1963.

[21] T. Irvine, *An Introduction to the Vibration Response Spectrum*, 2009.

[22] NanoAvionics, *Environmental Testing Requirements Falcon 9*, Jun. 2019.

[23] *NASA-STD-5002 | NASA Technical Standards System (NTSS)*, Sep. 2019.

[24] A. H. Hauglid, "Nonlinear Mechanical Vibrations: The Effect of Gaps," 2018.

[25] P. Bhatt, *Maximum Marks Maximum Knowledge in Physics*. Allied Publishers, 2010, ISBN: 978-81-8424-444-1.

[26] H. Jimin and Z.-F. Fu, *Modal Analysis*. Elsevier, 2001, ISBN: 0-7506-5079-6.

[27] C. F. Beards, *Structural Vibration : Analysis and Damping*. Elsevier, 1996.

[28] *ECSS-E-30 Part 2A – Mechanical – Part 2: Structural (25 April 2000). | European Cooperation for Space Standardization*.

[29] D. Wilson, *Vibration Testing for Small Satellites*, 1989.

[30] J. Alexander, "The Shock Response Spectrum – A Primer," in *Proceedings of the IMAC-XXVII, February 9-12, 2009 Orlando, Florida USA. Society for Experimental Mechanics*. Jun. 2009.

[31] T. Irvine, *An introduction to the shock response spectrum*, Sep. 2012.

[32] "Virgin Orbit SmallSat Launch Venture takes over LauncherOne Operation as Test Flights approach – Spaceflight101," Feb. 2017. [Online]. Available: `https://spaceflight101.com/virgin-orbit-takes-over-launcherone-project/` (visited on 04/19/2021).

[33] *What does 6 Degrees Of Freedom or 6-DOF mean?* [Online]. Available: `https://dragonflycv.com/what-does-6-degrees-of-freedom-or-6-dof-mean/` (visited on 05/13/2021).

[34] *NTNU SmallSat Lab*. [Online]. Available: `https://www.ntnu.edu/ie/smallsat/project-overview` (visited on 03/18/2021).

[35] T. H. Kaasa, M. Hjertenæs, E. F. Prentice, T. Tran, H. Galtung, and M. B. Henriksen, "HYPSO-DR-003: HSI Design Report," NTNU, Tech. Rep., Mar. 2020.

[36] W. Frei, *Meshing Your Geometry: When to Use the Various Element Types*, Apr. 2013. [Online]. Available: `https://www.comsol.com/blogs/meshing-your-geometry-various-element-types/` (visited on 04/30/2021).

[37] *Simcenter Nastran Element Library Reference*, 2019.

[38] S. Batchu, "Spring Elements In Nastran | Stress Ebook LLC.," Jun. 2015.

[39] SMAC, *SMAC Isolators Catalogue*.

[40] Q. Bianco, *ET23710-RE01 Design Justification Report*, Unpublished, Oct. 2020.

[41] T. Rølvåg, *Finite Element Dynamic Analysis*, Mar. 2018.

[42] *Simcenter 3D Pre/Post*. [Online]. Available: `https://docs.sw.siemens.com/en-US/product/289054037/doc/PL20200601120302950.advanced/html/id631266` (visited on 05/12/2021).

[43] E. Prentice, "HYPSO Mechanical Design & Testing; Environmental Testing," Nov. 2020.

[44] M. Hjertenæs, E. F. Prentice, and T. H. Kaasa, "HYPSO-TRP-VIB-002: Shock, Resonance, and Vibration of CLAW-1 EM," NTNU, Tech. Rep., May 2020.

[45] *What is a Frequency Response Function (FRF)?* Oct. 2020. [Online]. Available: `https://community.sw.siemens.com/s/article/what-is-a-frequency-response-function-frf` (visited on 05/10/2021).

Appendices

A FEM Tables

Point Masses

The point mass' coordinates is their CoM with regards to the BRF.

Table 1: Point mass overview

Point Masses			
Part	**Weight [g]**	**Connection**	**Coordinates [mm]**
Tuna Can 1	301.9	RBE3	*62.84, -0.09, -183.81*
Tuna Can 2	242.7	RBE3	*-60.55, -0.85, -183.44*
Magnetorquer 1	58.6	RBE3	*0.00, 0.00, -68.26*
Magnetorquer 2	48.5	RBE3	*-86.10, 40.24, -116.21*
Electronics Stack	1159.1	RBE3	*55.71, -0.09, -128.84*
Reaction Wheels	463.2	RBE3	*-86.16, 1.68, -118.01*
SBand Radio	192.2	RBE3	*-3.20, -17.50, -129.42*
Payload Controller	50.4	RBE3	*-98.80, 0.00, 55.65*
Star Tracker	108.0	RBE3	*62.17, 2.38, 118.10*
IMU	55.0	RBE3	*-43.44, -29.81, 127.69*
BoB	53.7	RBE3	*86.11, -0.15, 1.59*
HSI Detector	58.0	RBE3	*17.41, 1.65, -64.75*
RGB Detector	16.0	RBE3	*-46.04, 4.64, 106.45*
HSI Grating	8.0	RBE3	*2.65, 4.15, 30.55*

B List Of Components

Subsystems mech:design:comps [HYPSO Mechanical Design & Testing] (ntnu.no)						Weight in CAD			Point Masses
Components	No.	Edit	Materials	Weight [g]	Weight total [g]	Weight [g]	Total Weight [g]	Diff [g]	Coordinates [X, Y, Z]
Na Bus									
TunaCan 1	1	Point mass		301,90	301,90	301,90	301,90	0,00	(62.8413, -0.0888, -183.8127)
TunaCan 2	1	Point mass		242,70	242,70	242,70	242,70	0,00	(-60.5505, -0.8471, -183.4445)
Magnetorquer1	1	Point mass		58,60	58,60	58,60	58,60	0,00	(0.00, 0.00, -68.2649)
Magnetorquer 2	1	Point mass		48,50	48,50	48,50	48,50	0,00	(-86.0951, 40.2426, -116.2096)
Electronics Stack	1	Point mass		1159,10	1159,10	1159,10	1159,10	0,00	(55.7127, -0.0897, -128.8434)
Sband Radio	1	Point mass		192,20	192,20	192,20	192,20	0,00	(-3.2, -17.5, -129.417)
Reaction Wheels	1	Point mass		463,18	463,18	463,18	463,18	0,00	(-86.1598, 1.6782, -118.0097)
Payload Controler	1	Point mass		50,40	50,40	50,40	50,40	0,00	(-98.799, 0.0, 55.65)
6U Frame	1	Idealize	AA 7075-T7	718,20	718,20	718,20	718,20	0,00	
Sband Plate	1	Idealize	AA 7075-T7	60,90	60,90	61,10	61,10	-0,20	
3U Ring Frame	1	Idealize	AA 7075-T7	69,30	69,30	74,10	74,10	-4,80	
2U Ring Frame	1	Idealize	AA 7075-T7	71,20	71,20	61,80	61,80	9,40	
Solar Panel +X	1	Idealize	FR4	120,50	120,50	126,60	126,60	-6,10	
Solar Panel -X	1	Idealize	FR4	132,30	132,30	122,00	122,00	10,30	
Solar Panel +Y	1	Idealize	FR4	280,60	280,60	302,00	302,00	-21,40	
Solar Panel -Y	1	Idealize	FR4	287,10	287,10	302,00	302,00	-14,90	
Payload Structure									
HSI Platform	1	Idealize	AA 6082-T6	664,50	664,50	667,30	667,30	-2,80	
Dampers	8		SMACSIL	5,60	44,80	5,50	44,00	-36,80	
Dampers Base	8		AISI SS 304 Annealed			4,70	37,60		
Front Crosslink +X	1	Idealize	AA 6082-T6	31,80	31,80	32,70	32,70	-0,90	
Front Crosslink -X	1	Idealize	AA 6082-T6	31,30	31,30	32,20	32,20	-0,90	
Back Crosslink -X	1	Idealize	AA 6082-T6	79,60	79,60	78,60	78,60	1,00	
Back Crosslink +X	1	Idealize	AA 6082-T6	83,30	83,30	83,10	83,10	0,20	
Payload Imaging									
HSI Platform Brackets	3	Idealize	AA 6082-T6	29,60	88,80	28,40	85,20	3,60	
HSI Objectives	3	Idealize	AA 6061-T6	103,90	311,70	104,10	312,30	-0,60	
Slit Tube + ret. ring + adapter	1	Idealize	6061?)	43,20	43,20	44,20	44,20	-1,00	
Slit	1	Idealize	AA 6061-T6	2,80	2,80	3,10	3,10	-0,30	
HSI Detector Housing	1	Idealize	AA 6082-T6	82,60	82,60	108,70	108,70	-26,10	
RGB Detector Housing	1	Idealize	AA 6082-T6	45,40	45,40	44,40	44,40	1,00	
RGB Objective	1	Idealize	AA 6061-T6	64,00	64,00	69,30	69,30	-5,30	
RGB Platform Bracket	1	Idealize	AA 6082-T6	22,50	22,50	23,00	23,00	-0,50	
HSI Detector PCB	1	Point mass	FR4	58,00	58,00	58,00	58,00	0,00	(17.4069, 1.6533, -64.7537)
RGB Detector PCB	1	Point mass	FR4	16,00	16,00	16,00	16,00	0,00	(-46.0363, 4.6433, 106.45)
Star Tracker	1	Point mass	AA 7075-T6	108,00	108,00	108,00	108,00	0,00	(62.1708, 2.3842, 118.0975)
Inertial Measurement Unit	1	Point mass	AA 7075-T7	55,00	55,00	55,00	55,00	0,00	(-43.4398, -29.8077, 127.6904)
Hardware & Cables	0	Point mass		131,80	0,00	131,80	0,00	0,00	
Grating Casette									
Cassette Front	1	Idealize	AA 6082-T6	22,56	22,56	23,00	23,00	-0,44	
Cassette Back	1	Idealize	AA 6082-T7	22,20	22,20	22,60	22,60	-0,40	
Grating	1	Point mass		8,00	8,00	8,00	8,00	0,00	(2.65, 4.1533, 30.55)
Pico BoB									
BoB PCBs + M2.5x5	1	Point mass	FR4	79,75	79,75	79,75	79,75	0,00	(86.1136, -0.1484, 1.5932)
ShieldRails + 1U Frame	1	Idealize	AA 6082-T6	126,80	126,80	144,10	144,10	-17,30	
ShieldPlate + 1U Frame	1	Idealize	AA 6082-T6	102,20	102,20	109,10	109,10	-6,90	
Total Weight					6451,49		6573,63	-122,14	

Figure 1: List of all satellite components with respective data

C Mesh Convergence Plots

In the following result tables, modes 1 through 6 have been removed since these are related to the six DoF and are expected to be zero. The options are displayed from highest amount of elements to the lowest (left to right). The option in cursive is the element size we chose, and NOMTETT is an option where MTETT is turned off and seed size is a little smaller than the base seed.

Table 2: Mesh convergence study of the front payload assembly

Payload Front					
Mode	**Natural Frequency [Hz]**				
	Base x 0.4	**Base x 0.2**	***Base seed***	**Base x 1.4**	**Base x 1.8**
7	1193	1194	*1198*	1199	1207
8	1379	1383	*1388*	1398	1414
9	1682	1690	*1698*	1719	1751
10	3368	3412	*3451*	3564	3822
11	4833	4910	*4974*	5330	5694
12	5516	5656	*5679*	5697	5845
13	5670	5711	*5845*	6384	7015
14	6786	6806	*6830*	6889	7510

Table 3: Mesh convergence study of rear payload assembly

Payload Rear						
Mode	**Natural Frequency [Hz]**					
	Base x 0.4	**Base x 0.75**	**Base seed**	***Base x 1.4***	**Base x 2.0**	**NOMTETT**
7	4594	4648	4658	*4683*	4728	4746
8	4963	5017	5029	*5039*	5049	5111
9	6156	6177	6185	*6186*	6177	6265
10	9057	9184	9196	*9310*	9547	9373
11	10249	10280	10256	*10196*	10229	10442
12	10504	10535	10601	*10522*	10510	10713
13	12300	12319	12332	*12332*	12381	12380
14	13030	13050	13061	*13060*	13100	13098

Table 4: Mesh convergence study of the HSI cassette assembly

HSI Cassette						
Mode	**Natural Frequency [Hz]**					
	Base x 0.4	**Base x 0.7**	**Base seed**	**Base x 1.4**	**Base x 2**	***NOMTETT***
7	8485	8518	8545	8573	8644	*8537*
8	12856	12980	13063	13136	13380	*13102*
9	13931	14079	14149	14338	14398	*14256*
10	14769	14857	14902	14980	15090	*14888*
11	15173	15281	15347	15441	15652	*15379*
12	16317	16417	16462	16514	16623	*16420*
13	22334	22929	23192	23288	23452	*22991*
14	22993	23293	23675	23744	23911	*23320*

Table 5: Mesh convergence study of the HSI platform assembly

HSI Platform						
Mode	**Natural Frequency [Hz]**					
	Base x 0.4	**Base x 0.75**	**Base seed**	**Base x 1.6**	**Base x 2.2**	***NOMTETT***
7	355	357	358	360	361	*359*
8	412	414	415	417	418	*416*
9	516	518	520	522	523	*521*
10	637	641	643	647	649	*646*
11	725	728	730	733	735	*732*
12	878	880	882	885	887	*886*
13	1043	1046	1049	1053	1056	*1053*
14	1061	1065	1068	1072	1075	*1073*

Table 6: Mesh convergence study of the picoBoB assembly

PicoBoB						
Mode	**Natural Frequency [Hz]**					
	Base x 0.38	**Base x 0.63**	**Base seed**	**Base x 1.5**	**Base x 2**	***NOMTETT***
7	1448	1453	1461	1469	1476	*1467*
8	1488	1490	1494	1503	1504	*1505*
9	1736	1741	1747	1755	1761	*1754*
10	1797	1799	1801	1807	1816	*1802*
11	1955	1958	1964	1974	1975	*1978*
12	2602	2604	2608	2617	2629	*2609*
13	3011	3016	3024	3037	3059	*3023*
14	3101	3104	3108	3119	3134	*3114*

Table 7: Mesh convergence study of the frame assembly

Frame					
Mode	**Natural Frequency [Hz]**				
	Base x 0.4	**MTETT**	***Base x 0.7***	**Base seed**	**Base x 1.3**
7	322	326	*328*	333	348
8	367	374	*375*	383	405
9	419	424	*426*	432	441
10	536	550	*549*	563	593
11	570	578	*580*	589	615
12	710	728	*727*	746	790
13	716	731	*730*	747	791
14	797	806	*814*	829	857

D Modal Frequencies

Table 8: Modal frequencies of the fixed model

# Mode	Frequency	Damped Frequency	%Viscous	%Hysteretic	%X_Mass	%Y_Mass	%Z_Mass
* 1	2.343e+02	2.342e+02	0.00000	5.00000	0.01601	0.08236	26.81453
* 2	2.710e+02	2.709e+02	0.00000	5.00000	27.20022	0.01987	0.03360
* 3	3.207e+02	3.206e+02	0.00000	5.00000	0.00029	41.84937	0.03932
* 4	3.649e+02	3.648e+02	0.00000	5.00000	0.28044	0.34551	0.04807
* 5	4.070e+02	4.068e+02	0.00000	5.00000	0.00296	10.74611	1.22772
* 6	4.430e+02	4.429e+02	0.00000	5.00000	0.00703	0.73778	0.00055
* 7	5.212e+02	5.211e+02	0.00000	5.00000	0.01845	4.35523	6.71137
* 8	5.274e+02	5.272e+02	0.00000	5.00000	0.06734	4.78427	0.37283
* 9	6.104e+02	6.102e+02	0.00000	5.00000	0.00184	1.28101	0.17106
* 10	6.307e+02	6.305e+02	0.00000	5.00000	0.00134	0.00031	0.00626
* 11	7.064e+02	7.062e+02	0.00000	5.00000	0.00923	0.47611	0.12893
* 12	7.512e+02	7.509e+02	0.00000	5.00000	0.02054	3.56076	0.01501
* 13	8.180e+02	8.178e+02	0.00000	5.00000	0.00235	0.00300	0.43202
* 14	8.353e+02	8.350e+02	0.00000	5.00000	0.01187	0.01712	0.00220
* 15	8.986e+02	8.983e+02	0.00000	5.00000	0.09216	1.09503	0.22820
* 16	9.386e+02	9.383e+02	0.00000	5.00000	0.79909	0.02137	0.00298
* 17	9.620e+02	9.617e+02	0.00000	5.00000	1.70648	0.05464	0.00254
* 18	9.836e+02	9.833e+02	0.00000	5.00000	1.67997	0.15067	0.64023
* 19	1.018e+03	1.018e+03	0.00000	5.00000	0.06329	0.01665	0.06535
* 20	1.059e+03	1.059e+03	0.00000	5.00000	0.03706	0.45680	0.36487
* 21	1.093e+03	1.092e+03	0.00000	5.00000	0.00111	0.23146	0.00079
* 22	1.094e+03	1.094e+03	0.00000	5.00000	0.00111	0.22073	0.05066
* 23	1.133e+03	1.133e+03	0.00000	5.00000	0.37278	0.02855	0.02228
* 24	1.157e+03	1.157e+03	0.00000	5.00000	0.00063	0.00022	0.80513

Table 9: Modal frequencies of the test bench model

# Mode	Frequency	Damped Frequency	%Viscous	%Hysteretic	%X_Mass	%Y_Mass	%Z_Mass
* 1	2.231e+02	2.230e+02	0.00000	5.00000	35.87354	0.02649	0.92218
* 2	2.308e+02	2.307e+02	0.00000	5.00000	1.80235	0.04079	18.45959
* 3	3.073e+02	3.072e+02	0.00000	5.00000	0.00646	30.51237	0.03811
* 4	3.532e+02	3.531e+02	0.00000	5.00000	0.00240	0.19790	0.04558
* 5	3.854e+02	3.853e+02	0.00000	5.00000	0.02081	8.37784	0.22850
* 6	4.379e+02	4.377e+02	0.00000	5.00000	0.10755	0.31620	0.01225
* 7	4.814e+02	4.812e+02	0.00000	5.00000	22.31530	0.00375	0.56099
* 8	5.049e+02	5.048e+02	0.00000	5.00000	1.29433	0.13353	6.44296
* 9	5.150e+02	5.149e+02	0.00000	5.00000	0.49682	5.53815	0.20537
* 10	6.012e+02	6.010e+02	0.00000	5.00000	0.03962	0.72535	0.15167
* 11	6.259e+02	6.257e+02	0.00000	5.00000	0.01240	0.00003	0.01133
* 12	6.757e+02	6.755e+02	0.00000	5.00000	0.01660	1.04131	0.12884
* 13	7.208e+02	7.206e+02	0.00000	5.00000	0.09338	1.66038	0.00061
* 14	7.855e+02	7.853e+02	0.00000	5.00000	0.76107	0.00788	0.23340
* 15	8.161e+02	8.159e+02	0.00000	5.00000	0.03237	0.05280	0.35068
* 16	8.790e+02	8.787e+02	0.00000	5.00000	0.00115	0.09110	0.31312
* 17	8.831e+02	8.828e+02	0.00000	5.00000	0.00533	2.92873	0.43591
* 18	9.012e+02	9.009e+02	0.00000	5.00000	0.34887	0.33512	0.09850
* 19	9.143e+02	9.141e+02	0.00000	5.00000	0.16495	2.53264	0.11118
* 20	9.280e+02	9.277e+02	0.00000	5.00000	0.02540	0.02501	0.04731
* 21	9.368e+02	9.365e+02	0.00000	5.00000	0.10909	0.09088	0.53367
* 22	9.658e+02	9.655e+02	0.00000	5.00000	0.02284	0.07788	1.65130
* 23	9.863e+02	9.860e+02	0.00000	5.00000	0.12212	0.02400	0.37906
* 24	1.011e+03	1.010e+03	0.00000	5.00000	0.01707	0.08874	0.39000

Table 10: Modal frequencies of the damper model

# Mode	Frequency	Damped Frequency	%Viscous	%Hysteretic	%X_Mass	%Y_Mass	%Z_Mass
* 1	6.983e+01	6.981e+01	0.00000	5.00000	0.00339	0.04842	17.16040
* 2	7.107e+01	7.105e+01	0.00000	5.00000	18.48172	0.01328	0.00229
* 3	7.469e+01	7.467e+01	0.00000	5.00000	0.00947	17.83172	0.04296
* 4	1.370e+02	1.370e+02	0.00000	5.00000	0.00252	0.00173	0.25856
* 5	1.668e+02	1.668e+02	0.00000	5.00000	0.00093	0.00007	0.00004
* 6	2.557e+02	2.556e+02	0.00000	5.00000	0.03202	0.00279	0.00001
* 7	3.747e+02	3.745e+02	0.00000	5.00000	0.65136	24.85386	0.24017
* 8	3.972e+02	3.971e+02	0.00000	5.00000	17.85519	0.10802	0.07527
* 9	4.216e+02	4.215e+02	0.00000	5.00000	23.99968	1.27157	0.10131
* 10	4.534e+02	4.533e+02	0.00000	5.00000	0.00898	0.07347	0.00015
* 11	4.800e+02	4.799e+02	0.00000	5.00000	0.36799	1.26973	1.09445
* 12	5.124e+02	5.122e+02	0.00000	5.00000	0.03760	1.31748	4.44935
* 13	5.788e+02	5.786e+02	0.00000	5.00000	0.03682	0.36843	0.55036
* 14	6.474e+02	6.472e+02	0.00000	5.00000	0.00956	0.06801	0.00026
* 15	7.183e+02	7.181e+02	0.00000	5.00000	0.09419	0.51235	0.40079
* 16	7.584e+02	7.582e+02	0.00000	5.00000	0.47225	0.32046	0.02319
* 17	8.169e+02	8.166e+02	0.00000	5.00000	0.01753	0.02610	0.41093
* 18	8.608e+02	8.606e+02	0.00000	5.00000	0.15173	0.30634	0.23148
* 19	8.832e+02	8.830e+02	0.00000	5.00000	0.00388	2.80361	0.50822
* 20	9.010e+02	9.007e+02	0.00000	5.00000	0.25292	1.43008	0.88950
* 21	9.112e+02	9.109e+02	0.00000	5.00000	0.02974	1.22493	0.23811
* 22	9.262e+02	9.259e+02	0.00000	5.00000	0.00000	0.17636	0.02315
* 23	9.413e+02	9.410e+02	0.00000	5.00000	0.70235	0.10200	2.04042
* 24	9.513e+02	9.510e+02	0.00000	5.00000	0.00118	0.02418	0.59490

E Random Vibration PSD Plots

Below comes all our resultant plots from the random vibration simulations. Plots from the physical test data [2], [44] are also included for easy comparing. The test event values are given in chapter 5.5.1.

X-Direction, Physical Test (QM)

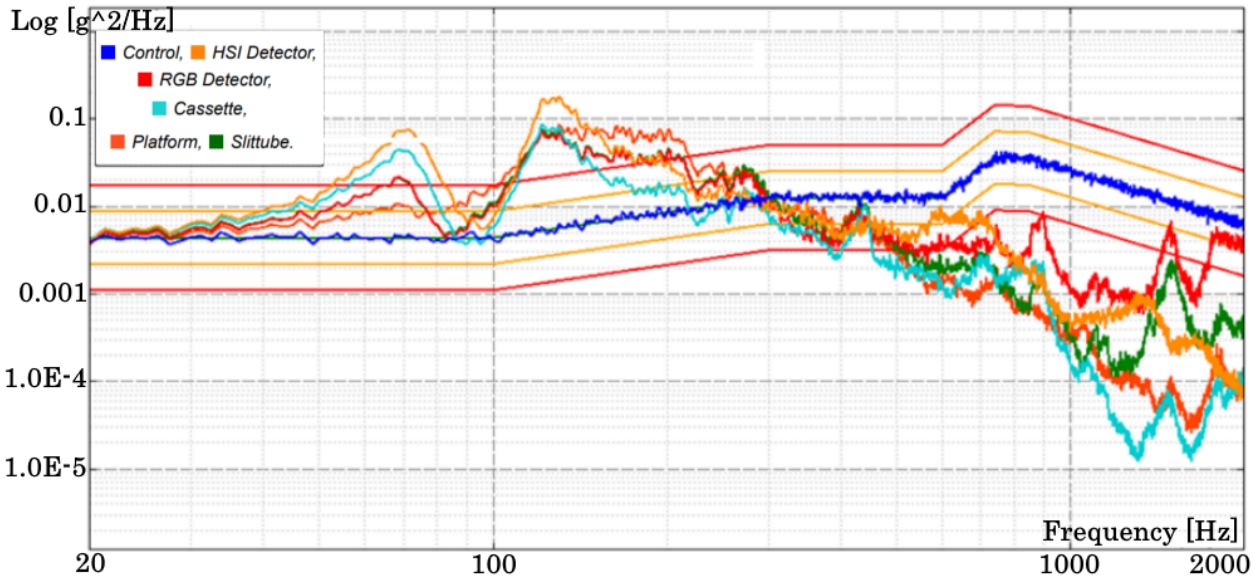

Figure 2: Random response of the QM for the physical random vibration test in the X-direction

X-Direction, Simulations

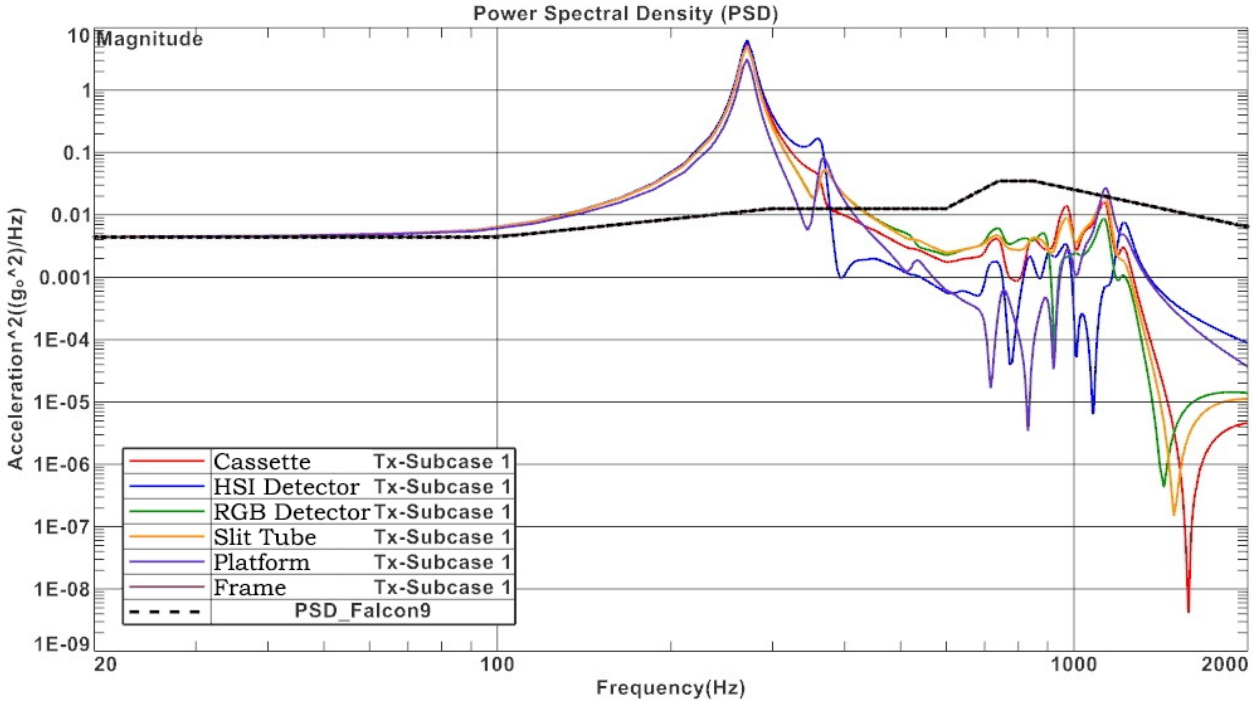

Figure 3: Random response in the X-direction from the fixed model in SOL 103 RS

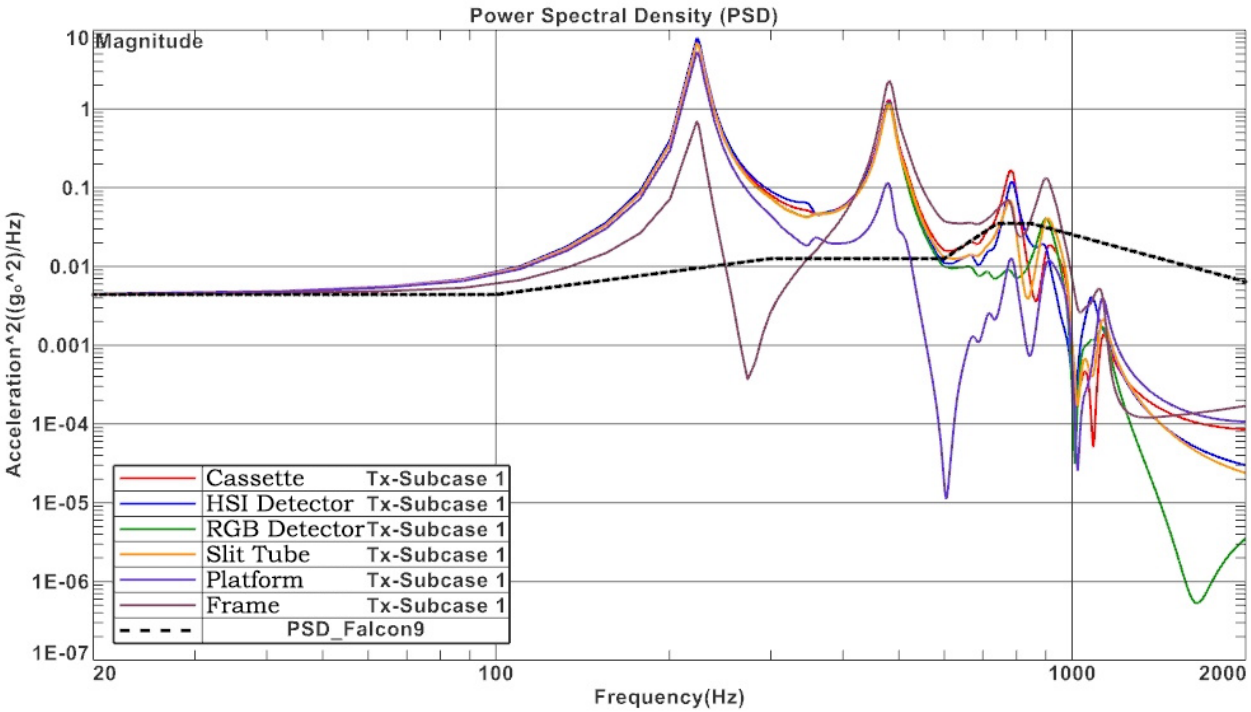

Figure 4: Random response in the X-direction from the test bench model in SOL 103 RS

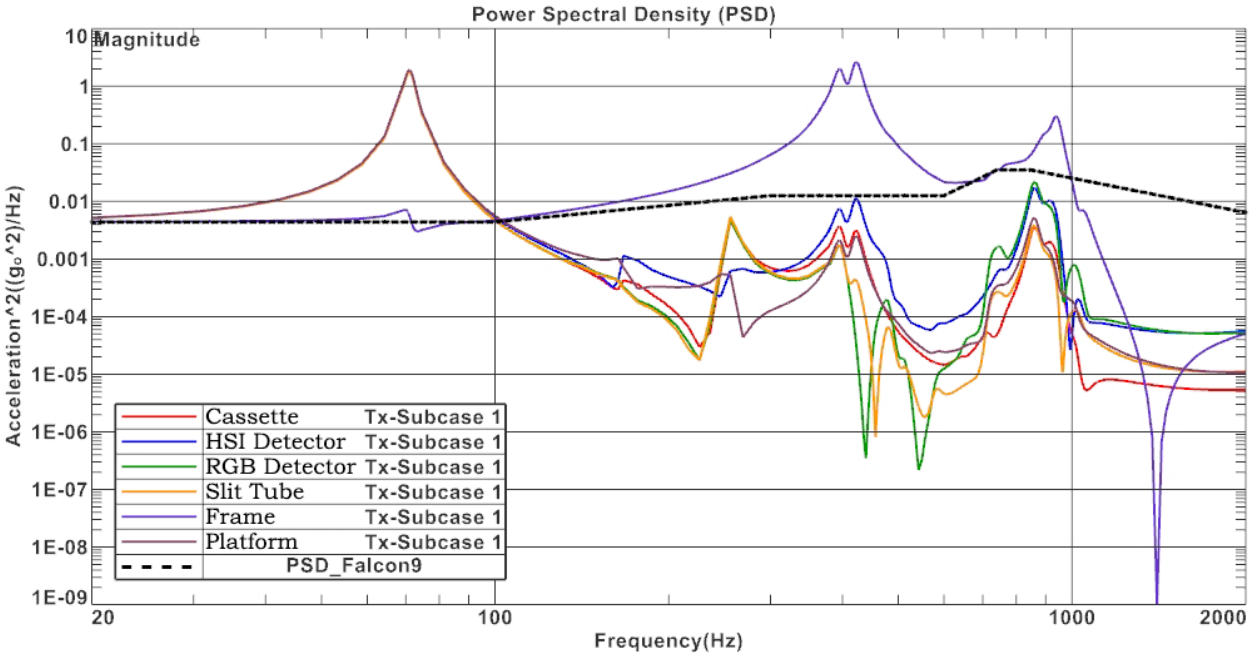

Figure 5: Random response in the X-direction from the damper model in SOL 103 RS

Y-Direction, Physical Test (QM)

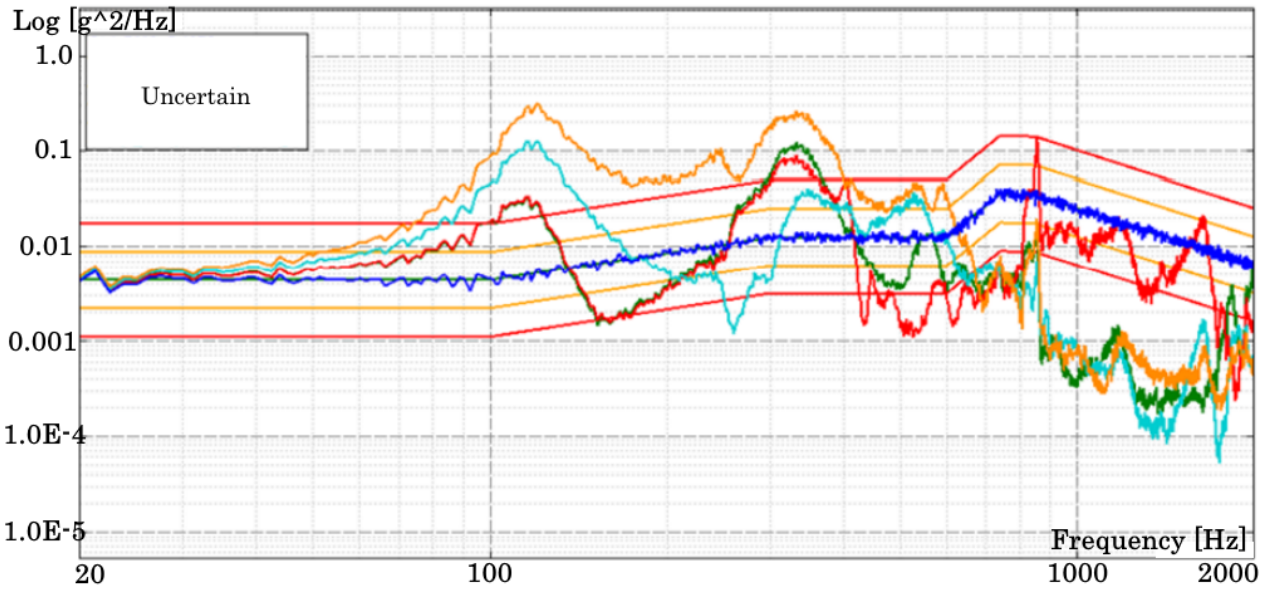

Figure 6: Random response of the QM for the physical random vibration test in the Y-direction

Y-Direction, Simulations

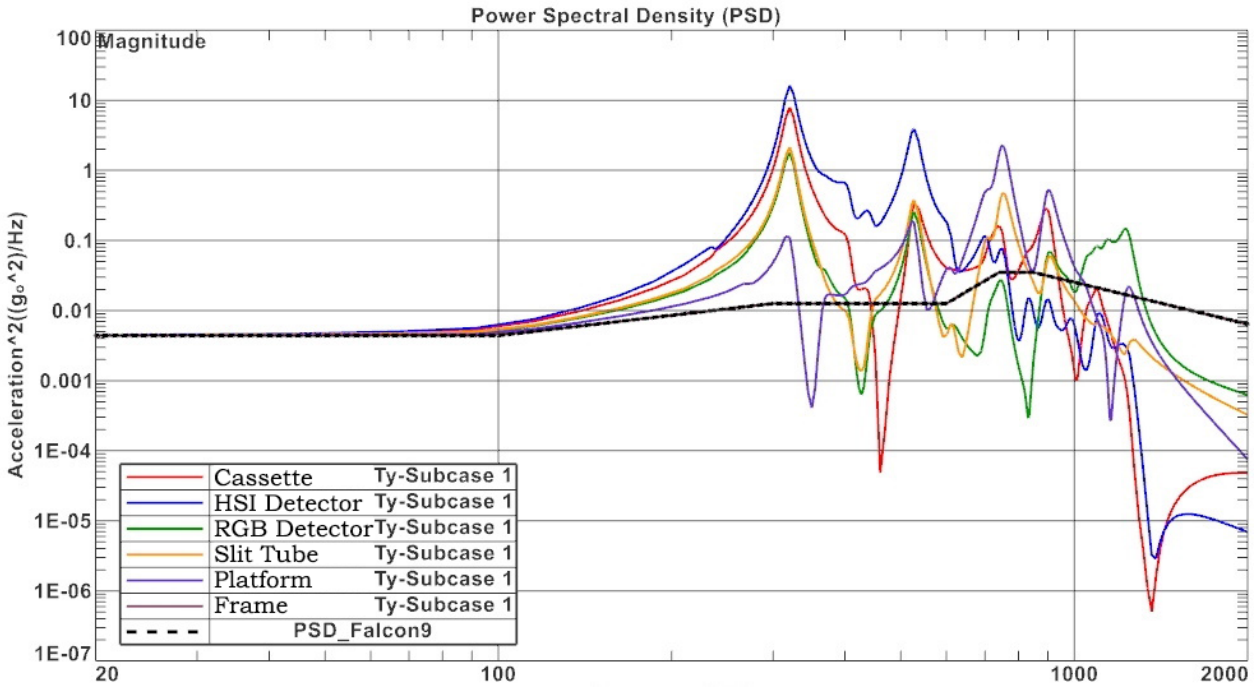

Figure 7: Random response in the Y-direction from the fixed model in SOL 103 RS

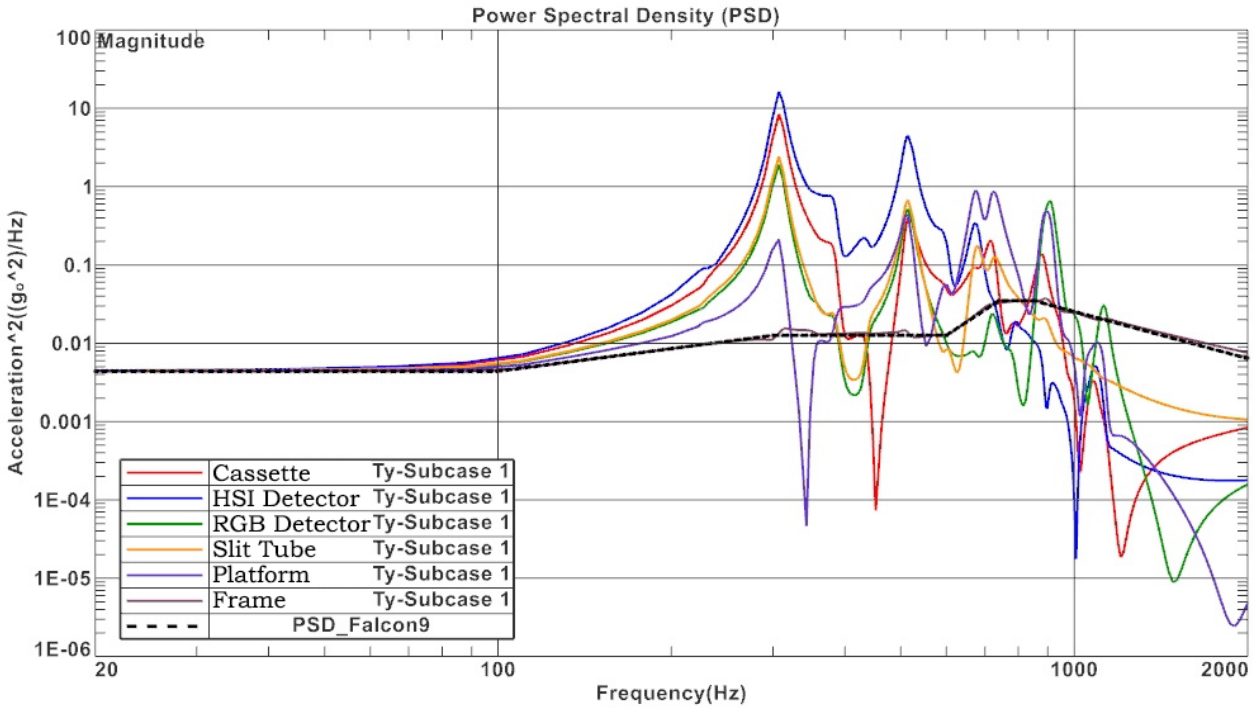

Figure 8: Random response in the Y-direction from the test bench model in SOL 103 RS

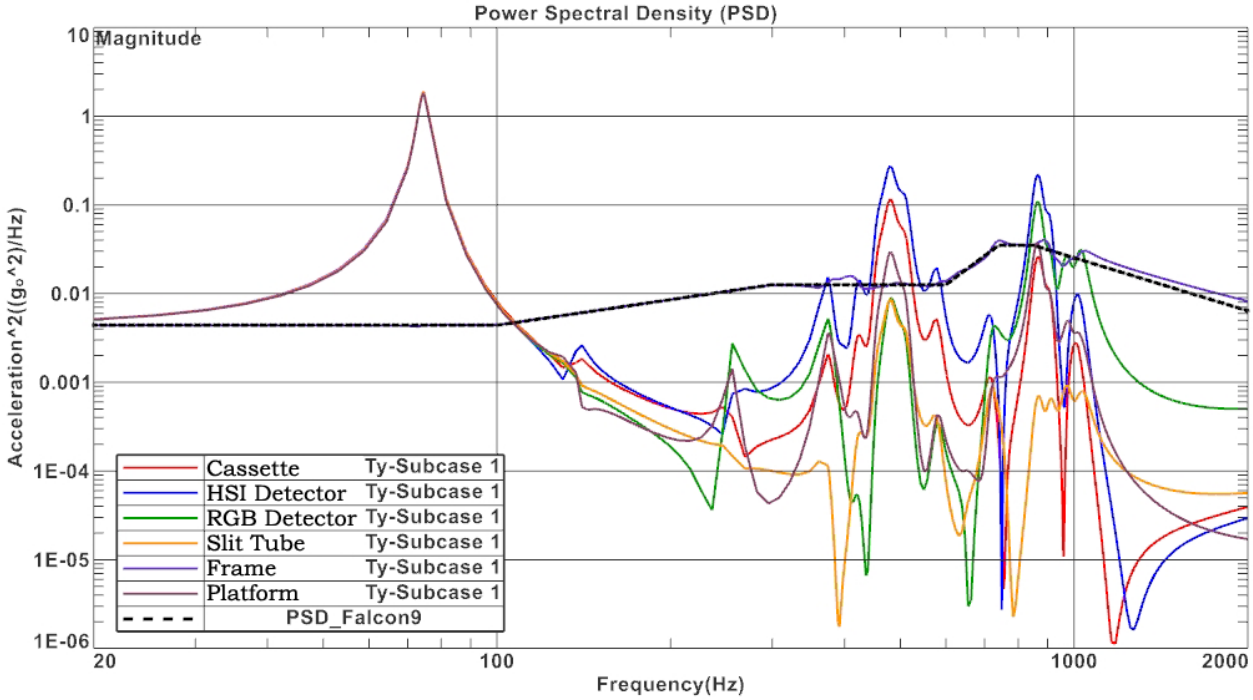

Figure 9: Random response in the Y-direction from the damper model in SOL 103 RS

Z-Direction, Physical Test (QM)

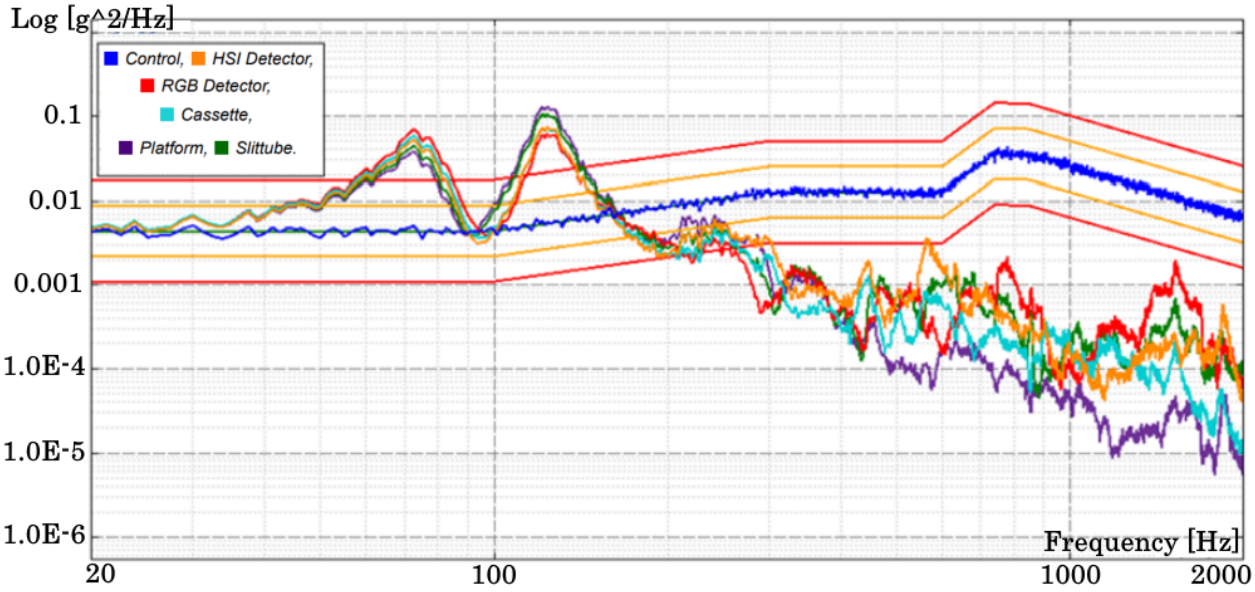

Figure 10: Random response of the QM for the physical random vibration test in the Z-direction

Z-Direction, Simulations

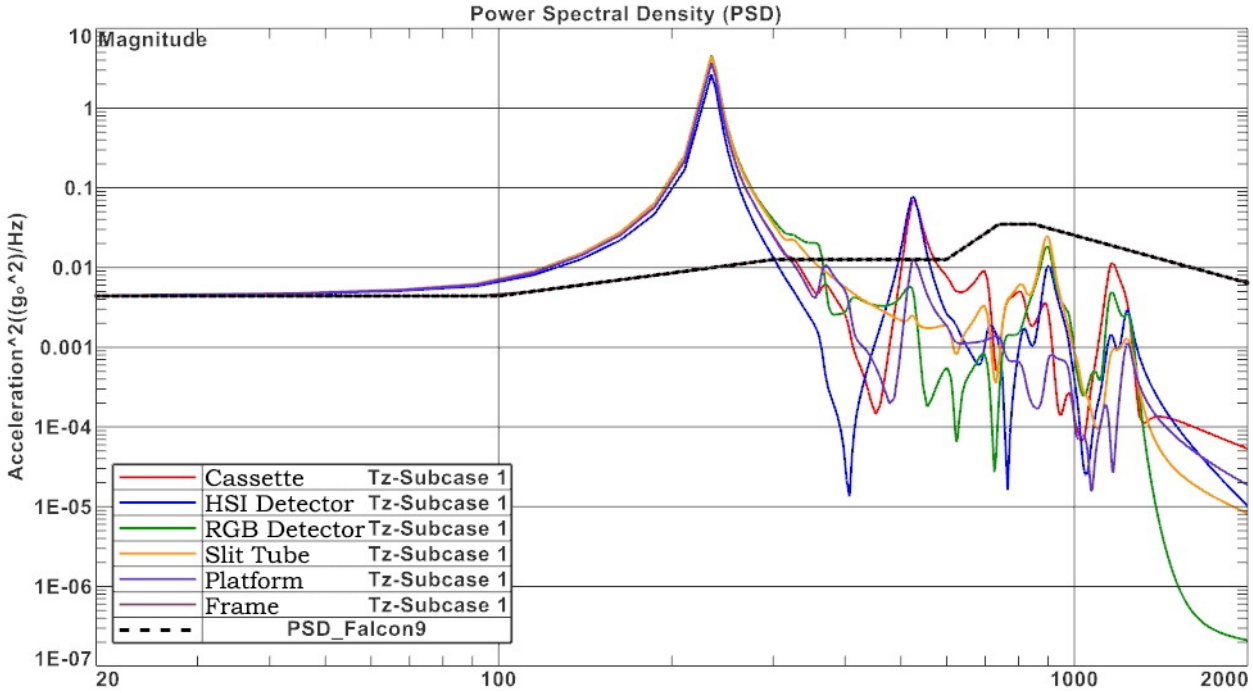

Figure 11: Random response in the Z-direction from the fixed model in SOL 103 RS

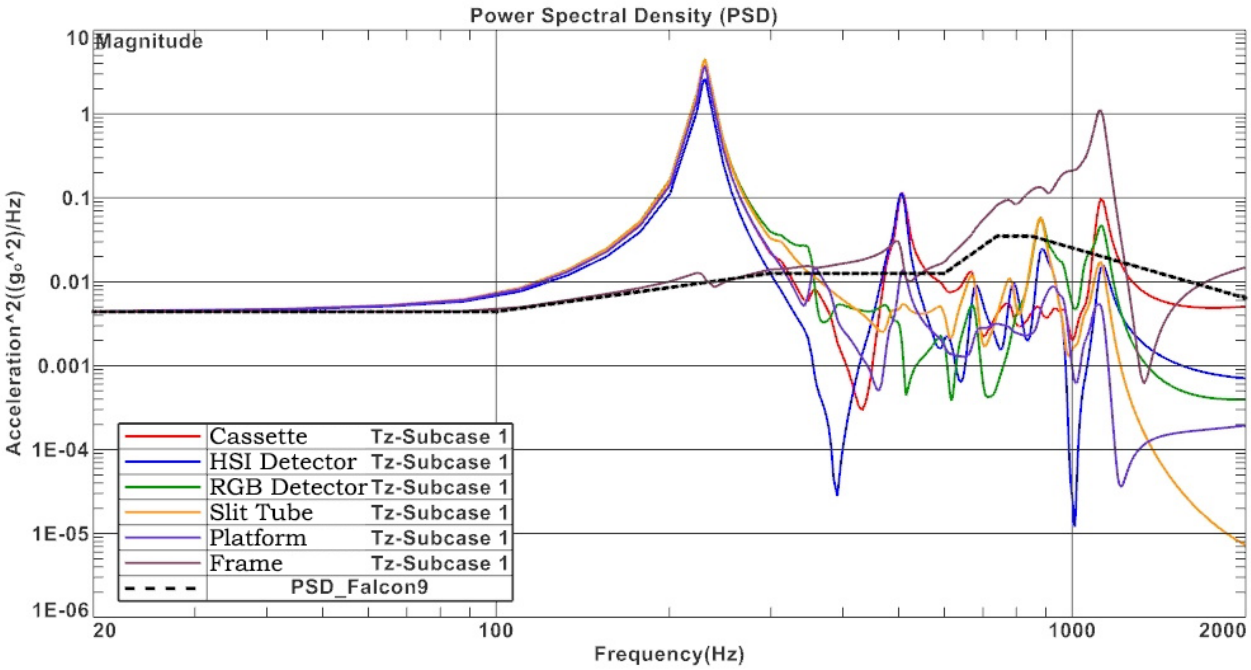

Figure 12: Random response in the Z-direction from the test bench model in SOL 103 RS

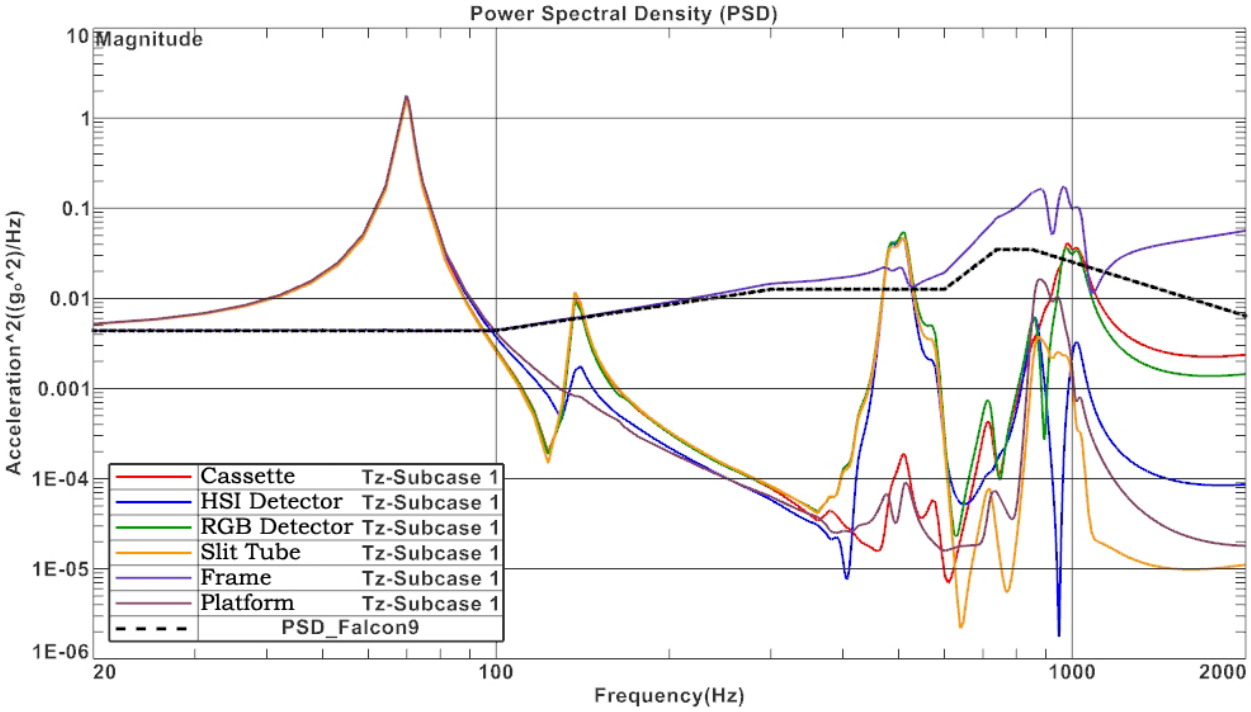

Figure 13: Random response in the Z-direction from the damper model in SOL 103 RS

F Physical Test SRS Plots

The following plots illustrate the SRS results from the HYPSO physical tests of the QM.

X-Direction

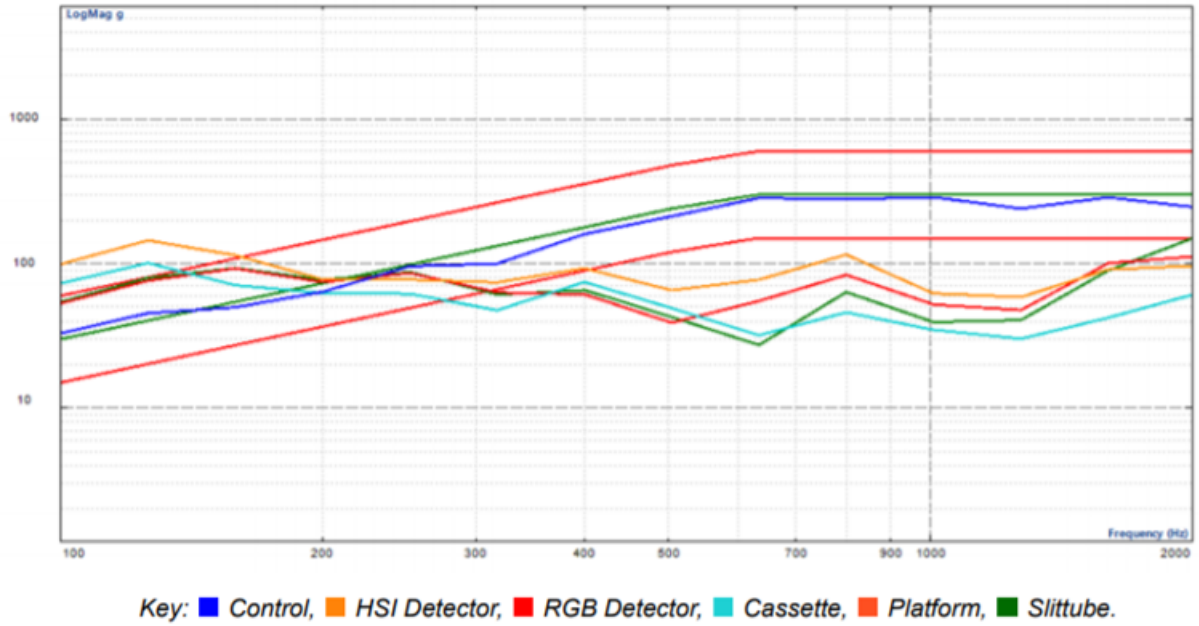

Figure 14: Shock response in x-axis from the physical testing

Y-Direction

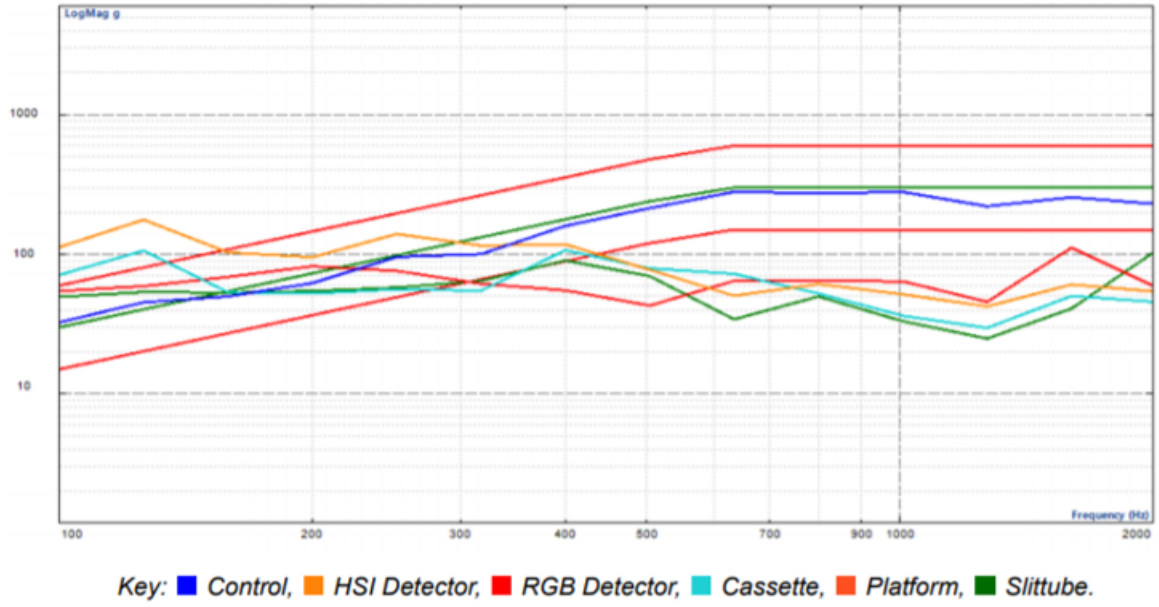

Figure 15: Shock response in z-axis from the physical testing

Z-Direction

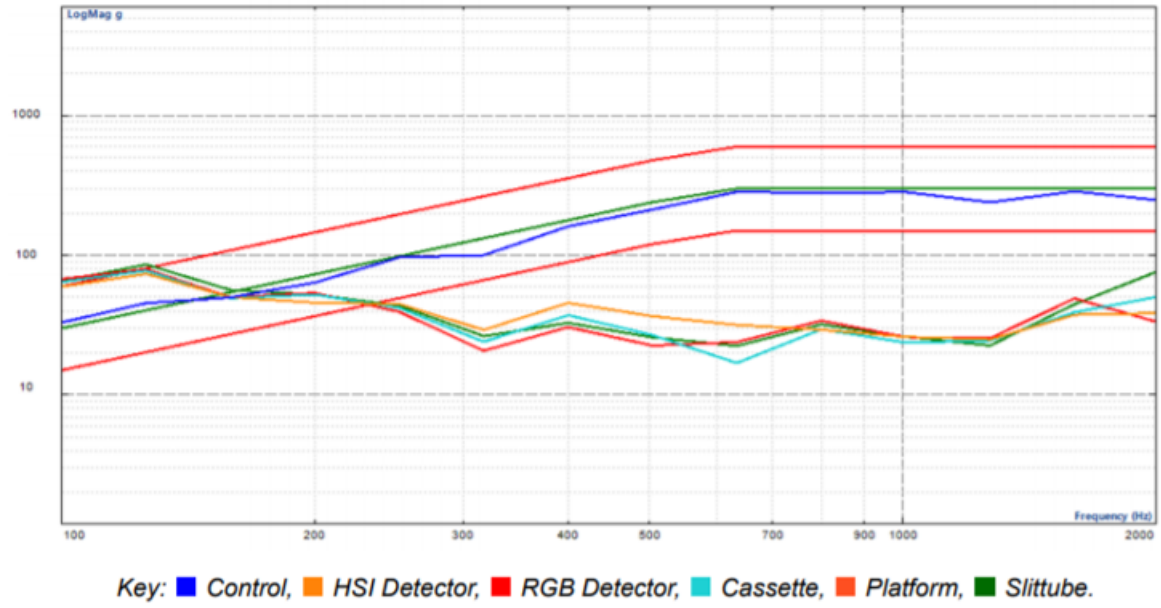

Figure 16: Shock response in z-axis from the physical testing

NTNU

Kunnskap for en bedre verden